AMERICAN SOCIETY FOR MICROBIOLOGY
Journals.ASM.org

Activation of Store-Operated Calcium Entry and Mitochondrial Respiration by Enterovirus 71 Is Essential for Efficient Virus Replication

Bang-Yan Hsu,[1] Ya-Hui Tsai,[2] Ta-Chou Weng,[1], Szu-Hao Kung[1]*

[1]Department of Biotechnology and Laboratory Science in Medicine, National Yang Ming Chiao Tung University, Taipei 112304, Taiwan.

[2]Department of Surgery, Far Eastern Memorial Hospital, Pan-Chiao, New Taipei, Taiwan.

*Address correspondence to Fourth Author: szkung@nycu.edu.tw

ABSTRACT

Enterovirus (EV) infections disrupt cellular calcium (Ca^{2+}) homeostasis. The EV protein 2B is localized to the endoplasmic reticulum (ER) and causes depletion of ER Ca^{2+} stores. This depletion coincides with a substantial increase in cytosolic Ca^{2+} levels driven by

extracellular Ca^{2+} influx. However, the precise mechanism underlying this influx remains elusive. In the present study, we demonstrated that EV71 infections induce store-operated Ca^{2+} entry (SOCE) by activating the Ca^{2+} sensor stromal interaction molecule 1 (STIM1), which subsequently interacts with Orai1, a plasma membrane (PM) Ca^{2+} channel. This finding was supported by confocal imaging, which revealed that STIM1, typically localized in the ER, becomes active and colocalizes with Orai1 at the PM in EV71-infected cells. Pharmacological inhibition of the STIM1–Orai1 interaction and knockdown of either STIM1 or Orai1 significantly reduced virus-induced cytosolic Ca^{2+} levels and viral replication. Global transcriptome analysis revealed that differentially expressed genes are primarily associated with the mitochondrial electron transport chain (ETC) upon SOCE activation, contributing to enhanced ATP generation and oxygen consumption. This increase in mitochondrial Ca^{2+} levels is correlated with the mid-stage of virus infection. Furthermore, we demonstrated that high levels of mitochondrial Ca^{2+} influx led to apoptotic cell death favoring viral release at the late stage of virus infection. Finally, SOCE-dependent EV replication was observed in a mouse intestinal organoid culture, a more physiologically relevant cell system. Our results provide valuable insights into the mechanism through which EV infections induce SOCE-mediated spatial and temporal control of Ca^{2+} signaling, substantially affecting the virus life cycle.

IMPORTANCE

Host cell Ca^{2+} signals play crucial roles in various steps of virus life cycles, including entry, replication, and exit. EV requires increased cytosolic Ca^{2+} levels for efficient replication, but the precise mechanisms underlying the association between Ca^{2+} levels and EV replication remain elusive. Using EV71 as a model virus, we demonstrated that EV71 infection elevated cytosolic Ca^{2+} levels through store-operated Ca^{2+} entry activation and progressive Ca^{2+} mobilization to mitochondria. This led to the upregulation of electron transport chain activity, which is essential for efficient virus replication and apoptotic cell death, facilitating viral release during the mid and late stages of the infectious cycle, respectively. These findings substantially enhance the understanding of how EVs co-opt host cell mechanisms to promote their own life cycle. STIM1 and Orai1 may be novel targets for broad-spectrum host-directed therapeutics against EVs and other viruses that employ similar replication mechanisms.

INTRODUCTION

Enteroviruses (EVs) are nonenveloped, positive-strand RNA viruses belonging to the genus *Enterovirus* of the family *Picornaviridae*. EVs consist of many human pathogens, including poliovirus, coxsackie A and B viruses, echoviruses, numbered EVs, and

48 rhinoviruses [1]. Diverse EVs can cause a wide array of clinical manifestations ranging
49 from mild illnesses to more severe and even life-threatening diseases, such as myocarditis,
50 meningitis, encephalitis and acute paralysis. Among EVs, EV71 (or EV-A71) infections
51 have caused several outbreaks of hand, foot and mouth disease, with a notable proportion
52 of infected infants and young children manifesting severe neurological complications and
53 even consequent death, mainly in the Asia-Pacific region [1, 2]. However, currently, there
54 are no approved antiviral agents available against EV infections.

55 Intracellular calcium (Ca^{2+}) concentration plays a crucial role in regulating various
56 cellular functions involved in physiological and pathological states. Viruses, as obligate
57 intracellular parasites, have developed strategies to manipulate Ca^{2+} signaling and
58 Ca^{2+}-dependent processes to promote their own life cycles [3, 4]. During the course of EV
59 infection, a gradual increase in the cytosolic Ca^{2+} level was observed, due partly to the
60 increased permeability of the endoplasmic reticulum (ER) and the consequent depletion
61 of Ca^{2+} stores in the ER, causing outflow of stored Ca^{2+} into cytoplasm [5, 6, 7, 8, 9]. In
62 addition, the influx of extracellular Ca^{2+} into EV-infected cells is thought to contribute to
63 increased cytosolic Ca^{2+} concentrations as well [7, 10]. Disruption in Ca^{2+} homeostasis
64 caused by EV infection is pivotal in viral replication. The use of Ca^{2+} chelators was
65 reported to substantially reduce the production of viral proteins and progeny viruses [11].
66 Studies have demonstrated that EV 2B proteins play a pivotal role in increasing cytosolic

67 Ca^{2+} levels. These proteins act as viroporins, a type of virus-encoded pore-forming

68 protein [12, 13, 14]. EV 2B proteins are small, integral membrane polypeptides consisting

69 of approximately 99 amino acids. They contain two hydrophobic regions connected by a

70 short stem-loop. One of these hydrophobic regions is likely to form an amphipathic alpha

71 helix, whereas the other is likely to form a complete hydrophobic helix. This

72 helix–loop–helix motif of 2B is believed to be responsible for its ability to form

73 transmembrane pores through oligomerization [12]. In EV-infected cells, 2B proteins

74 localize in membranes derived from the ER and Golgi apparatus. The pore-forming

75 activity of 2B in these organelle membranes results in a decrease in Ca^{2+} stores in the ER

76 and Golgi apparatus [10, 12], and is thus functionally associated with viral replication and

77 release [8, 10, 15]. The single expression of EV 2B is sufficient to recapitulate the changes

78 in Ca^{2+} homeostasis observed in EV-infected cells [7, 8]. However, the molecular

79 mechanism underlying the EV 2B–induced increase in cytosolic Ca^{2+} levels that supports

80 viral replication and release remains elusive.

81 The coordinated regulation of Ca^{2+} release from the ER and subsequent entry of Ca^{2+}

82 across the plasma membrane (PM) to replenish ER stores is referred to as store-operated

83 calcium entry (SOCE). SOCE is a homeostatic cellular mechanism that helps maintain

84 appropriate Ca^{2+} levels in the ER to facilitate Ca^{2+}-mediated signaling [16]. Two protein

85 families, stromal interaction molecules (STIMs) and Ca^{2+} release-activated Ca^{2+}

86 modulators (Orais), are responsible for activating SOCE [16, 17]. STIM proteins act as
87 sensors for Ca^{2+} levels in the ER. When Ca^{2+} is depleted in the ER [18], STIM proteins
88 aggregate into multiple puncta that translocate close to the PM. Orai, an essential
89 pore-forming component of SOCE, translocates to the same STIM-containing structures
90 during Ca^{2+} depletion in the ER and mediates extracellular Ca^{2+} entry. To date, three
91 isoforms of Orai (1–3) and two isoforms of STIM (1 and 2) have been identified in
92 mammals. STIM1 levels are higher than STIM2 levels in most tissues. Moreover, STIM1
93 and Orai1 are sufficient for the generation of Ca^{2+}-release-activated Ca^{2+} currents, making
94 Orai1 the primary channel activated by Ca^{2+} store release and STIM1 activation [19].

95 Given that EV 2B protein resides in the ER and that EV-infected or 2B-expressing cells
96 experience an influx of extracellular Ca^{2+}, we investigated whether the ER–PM
97 connection is involved in the increased cytosolic Ca^{2+} levels in the presence of EV 2B, i.e.,
98 SOCE activation, is involved in increased cytosolic Ca^{2+}. In the present study, we used
99 EV71, known to cause disrupted Ca^{2+} homeostasis, as a model [20, 21]. We demonstrated
100 that EV-infected cells activate SOCE, with this activation mediated by the interaction
101 between STIM1 and Orai1. To understand the downstream Ca^{2+} signaling events that
102 support viral replication, we performed bulk RNA-sequencing (RNA-seq) to analyze the
103 transcriptome of EV71-infected cells and the transcriptional reprogramming of a specific
104 SOCE inhibitor, AnCoA4. We determined that SOCE activation led to an increase in

105 mitochondrial Ca^{2+} levels, thereby promoting ATP production and cellular respiration by
106 transcriptionally upregulating a panel of genes encoding mitochondrial electron transport
107 chain (ETC) complexes at 6 h postinfection (p.i.). Treatment with oligomycin, an inhibitor
108 of ATP production, reduced viral replication in a dose-dependent manner, indicating that
109 increased ATP production is required for efficient EV71 replication. At 12 h p.i., Ca^{2+}
110 influx led to mitochondrial Ca^{2+} overload, resulting in the activation of intrinsic apoptosis
111 that facilitated virus egress and pathogenesis. This SOCE and mitochondria
112 Ca^{2+}-dependent viral replication phenomenon was also noted in other EV serotypes.
113 Finally, we observed SOCE-dependent upregulation of ETC complexes and EV replication
114 in a mouse intestinal organoid culture, a physiologically-relevant model known for its
115 prior uses in studies of cell Ca^{2+} flux and mitochondrial respiration [22, 23, 24].

116 # MATERIALS AND METHODS

117 ## Cells and Viruses

118 Rhabdomyosarcoma (RD) cells (ATCC, CCL-13) and HeLa cells (ATCC, CCL-2) were
119 cultured as described elsewhere [25]. Human EV stocks used in this study included EV71
120 (strain BrCr), coxsackievirus A16 (CVA16), CVB3 and echovirus serotype 30 (Echo30) as

121 reported previously [25]. A mouse-adapted EV71 MP4 strain [26] was provided by Dr.
122 Jen-Ren Wang (National Cheng Kung University, Taiwan). All virus stocks were titrated
123 on RD cells by 50% tissue culture infectious dose ($TCID_{50}$) assay.

124 **Ca^{2+} fluorescence dyes assay**

125 RD and HeLa cells were infected with EV71 at a specified multiplicity of infection
126 (MOI) in 24-well plates for the indicated durations. Cells were incubated with the
127 cytosolic Ca^{2+} dye Fluo-8 at 1 μM or the mitochondrial Ca^{2+} dye Rhod-2 AM at 3 μM,
128 both for 30 min at 37°C. The emitted fluorescence resulting from Fluo-8 or Rhod-2 AM
129 staining was observed using a fluorescence microscope (Leica DM6000B) with a 488-nm
130 or 543-nm filter, respectively. The fluorescence intensity was quantified using MetaMorph
131 software (Molecular Devices, Downington, PA).

132 **Ectopic expressions of STIM1 and Orai1 for confocal analysis**

133 Plasmid encoding enhanced green fluorescent protein (EGFP)-labeled STIM1
134 (pEGFP-STIM1) and monomeric red fluorescent protein (mOrange)-labeled Orai1
135 (pmOrange-Orai1) were provided by Dr. Meng-Ru Shen (National Cheng Kung

136 University, Taiwan). The colocalization of STIM1 and Orai1 was observed by confocal

137 microscopy. See Text S1 for details.

138 **RNA-seq**

139 RD cells were infected with EV71 at an MOI of 0.5 for 6 h in the presence of DMSO or

140 20μM AnCoA4. RNA extraction was performed using RNeasy Kits (Qiagen, Hamburg,

141 Germany), and RNA-seq libraries were prepared using the Universal Plus mRNA Seq

142 Preparation kit (Tecan). RNA-seq was performed using the NovaSeq 6000 platform

143 (Illumina, San Diego, CA) in accordance with the manufacturer's protocol, with 2 ×

144 150-bp paired-end sequencing. Reads were aligned to the GRCm38 build of the human

145 genome by using CLC Genomics Workbench v10 (Qiagen).

146 **Differential expression analysis**

147 The expression level of each gene was examined by fragment length, determined by

148 read counts, and normalized using the fragments per kilobase of transcript per million

149 mapped fragments variation method. Genes with significant changes in mRNA levels

150 were identified on the basis of a false discovery rate cutoff of 0.05 and a fold change of 2.

151 Gene set enrichment analysis was conducted using the Database for Annotation,

152 Visualization, and Integrated Discovery (DAVID, https://david.ncifcrf.gov/) [27].

153 Biological processes with corrected *p*-values of ≤0.05 were considered significantly

154 enriched pathways.\

155 **Measurement of cellular respiration**

156 Cellular respiration was measured using the Seahorse XF Cell Mito Stress Test Kit

157 (Agilent, Santa Clara, CA) in accordance with the manufacturer's instructions. HeLa cells

158 seeded in XFe 24-well microplates were infected with EV71 stock at an MOI of 5 for 6 h.

159 The microplates were placed in a non-CO_2 incubator at 37°C for 1 h prior to measurement.

160 Cellular respiration was analyzed using sequential injections of 2 μM oligomycin (an ATP

161 synthase blocker), 1 μM carbonyl cyanide-p-trifluoromethoxyphenylhydrazone (FCCP, an

162 activator of the uncoupling of the inner mitochondrial membrane), and 0.5 μM

163 rotenone/antimycin A (inhibitors of complexes I and III). The oxygen consumption rate

164 (OCR) was determined by Seahorse XFe24 Extracellular Flux Analyzer (Agilent).

165 **Cultivation, infection and imaging of crypt organoids**

166 Mouse intestinal stem cells were isolated following a method documented [28] and it
167 is reported in the Text S1. The preparation and culture of mouse intestinal organoid
168 followed a protocol described previously with certain modifications [22]. Briefly, mouse
169 crypt organoids were seeded in differentiation medium consisting of Advanced
170 DMEM/F12 (Invitrogen) containing growth factors as previously reported [28]. Crypt
171 organoids were mixed with Matrigel (BD Bioscience) and plated in 12-well plates. The
172 medium was changed every 2 days for 10-14 days. Differentiated mouse intestinal
173 organoids were sheared mechanically by pipetting to enable sufficient apical exposure to
174 virus inoculums. The organoids were inoculated with 200 μL EV71 MP4 strain (4×10^8
175 $TCID_{50}$/mL) for 2 h at 37°C. After the incubation, the organoids were washed with PBS
176 and organoids were embedded in Matrigel with the differentiation medium at 37 °C for 48
177 h. The images were acquired by confocal microscopy (LSM880, Zeiss). See Text S1 for
178 details.

179 # RESULT

180 ## EV71 infection induced Ca^{2+} influx that is required for efficient virus replication

181 Previous studies have demonstrated that infection with poliovirus or coxsackievirus B
182 increases cytosolic Ca^{2+} levels [5, 6]. In the current study, we used EV71 as a model virus
183 due to its known activities in triggering Ca^{2+} flux and Ca^{2+}-dependent signaling [20]. To
184 investigate the Ca^{2+} flux and its impact on EV71 replication in a single-cycle infection, RD
185 cells were infected with EV71 at a lower or a higher dose, i.e., an MOI of 0.5 or 5,
186 respectively, for 12 h. Our results revealed that the cytosolic Ca^{2+} levels significantly
187 increased starting at 4 or 6 h p.i. upon 0.5- or 5-MOI infection, respectively, and continued
188 to rise throughout the infection, as indicated by staining with the fluorescent
189 Ca^{2+}-binding dye Fluo-8 (Fig. 1A, 1C). To further identify the source of Ca^{2+}, we added
190 intracellular and extracellular Ca^{2+} chelating agents, BAPTA-AM (referred to as BAPTA
191 hereafter) and EGTA, respectively, both at non-cytotoxic concentrations (Fig. S1). At 0.5
192 MOI infection, both treatments resulted in a marked reduction in cytosolic Ca^{2+} levels
193 between 6 and 12 h p.i. (Fig. 1A, S2), indicating that at least part of the increased cytosolic
194 Ca^{2+} originated from outside the infected cells in this condition. Viral titers were also
195 reduced upon the treatments at all points tested during the infection (Fig. 1B). On the
196 other hand, infection at 5 MOI led to a significant reduction in the cytosolic Ca^{2+} only at 4

197 and 6 h p.i., and Ca^{2+} raised to the levels indistinguishable from that of the controls for

198 the remaining infection period (Fig. 1C). A similar trend of virus replication kinetics in

199 HeLa cells upon the Ca^{2+} chelator treatments was observed (Fig. S3). In line with the

200 finding, viral replication was significantly delayed at 4 and 6 h p.i. by the treatment of the

201 Ca^{2+} chelating agents but not thereafter. This implies that EV71 infection at 5 MOI

202 resulted in the induction of cytosolic Ca^{2+} to the high levels that are not susceptible to the

203 treatments of the Ca^{2+}-chelators late in the infection (9 and 12 h p.i.). Together, these data

204 indicate that extracellular Ca^{2+} influx contributed to the increase in cytosolic Ca^{2+}

205 observed during EV71 infection and that the increase in cytosolic Ca^{2+} level is correlated

206 with the progression of viral replication, consistent with that for other EVs [5, 6].

207 **Orai1 and STIM1 are essential during active replication of EV71**

208 Several Ca^{2+} channels or transporters on the PM mediate Ca^{2+} influx from outside the
209 cells [29]. Among them, only SOCEs are activated by the link between ER-resident STIM1
210 and PM-resident Orai1. EV 2B localizes in the ER and reduces ER Ca^{2+} levels by forming
211 transmembrane pores [30]. Thus, we hypothesized that SOCE machinery contributes to
212 Ca^{2+} influx extracellularly through the PM, resulting in the observed increase in cytosolic
213 Ca^{2+} levels in the EV71-infected and 2B-expressing cells.

214 To validate this hypothesis, we first investigated EV71 infection at 6 h p.i., a time point
215 that the increased cytosolic Ca^{2+} and viral replication were most sensitive to the Ca^{2+}
216 chelating agents (Fig. 1B, D), upon the treatment of a specific SOCE blocker AnCoA4
217 [31]at 10- and 20-μM in RD cells. Dose-dependent reduction in viral titers was found,
218 with viral replication reduced for about a log by 20 μM AnCoA4 (Fig. 2A). For infection
219 with 0.5 MOI, we observed that levels of cytosolic Ca^{2+} were significantly reduced from 6
220 h to 12 h p.i., similar to those treated by Ca^{2+} chelation (Fig. 1A, 2B). The viral titers were
221 significantly reduced at all time points during the infection period (Fig. 2C) For cells
222 infected with EV71 at 5 MOI, on the other hand, a significant reduction in cytosolic Ca^{2+}
223 and viral titers by AnCoA4 were limited to 4 h and 6 h p.i., and the antiviral effects
224 significantly attenuated with viral titers reaching comparable levels between the treated-

225 and control groups at 9 h and 12 h p.i. (Fig. 2D, E). This finding is consistent with those
226 treated with the Ca^{2+} chelating agents (Fig. 1, S3). A similar trend of virus replication in
227 HeLa cells upon AnCoA4 treatment was noted (Fig. S3) To identify the stage of viral
228 replication promoted by SOCE, we performed a time-of-addition experiment with the
229 treatment of AnCoA4 during distinct stages of virus infection (Fig. 2F, G). Based on the
230 total virus titer determined from each condition, we concluded that AnCoA4 treatment
231 during 3-6 h after viral adsorption, but not other stages tested, displayed significant
232 inhibition on virus replication.

233 To gain more insights into the role of SOCE in EV71 infection, we used
234 lentivirus-mediated RNA interference to generate stable STIM1- and Orai1-knockdown
235 cells, and the efficient knockdown effects were validated (Fig. S4). Knockdown of either
236 STIM1 or Orai1 resulted in marked reductions in EV71-induced cytosolic Ca^{2+} at 6 h p.i.
237 and 12 h p.i., compared with that of the scramble control (Fig. 3A). Likewise, levels of
238 viral protein and viral titers were greatly reduced in the STIM1- and Orai1-knockdown
239 cells over the scramble controls, at both 6 h p.i. and 12 h p.i. (Fig. 3B, C).

240 Subsequently, we generated HeLa cells ectopically coexpressing STIM1 and Orai1
241 labeled with EGFP and mOrange, respectively (Text S1). Transfection of EV71 2B was
242 conducted because single expression of EV 2B expression was sufficient to induce the

243 influx of extracellular Ca^{2+} and to release Ca^{2+} from ER stores [10]. Thapsigargin (TG)
244 was used as a control as it is known to induce ER Ca^{2+} store depletion and activate SOCE
245 by blocking the sarco/ER Ca^{2+}-ATPase pump [32]. Whereas the mock-infected and
246 empty-plasmid cells exhibited minimal levels of STIM1-Orai1 colocalization, the infected
247 HeLa-Orai1-STIM1 cells (Fig. 4A) or the cells ectopically expressing viral 2B (Fig. 4B, D)
248 exhibited increased colocalization of STIM1 and Orai1, consistent with that of the
249 TG-treated cells (Fig. 4A, B). Moreover, the colocalization of STIM1 and Orai1 caused by
250 EV71 infection was substantially inhibited by the treatment of AnCoA4 (Fig. 4A). In all
251 cases, colocalization between EGFP-STIM1 and mOrange-Orai1 was quantified by
252 calculation of Mander's coefficient [33] (Fig 4C, D).

253 Taken together, these data indicated that EV71 infection activated the STIM1-Orai1
254 machinery, resulting in increased cytosolic Ca^{2+}, which is essential for active virus
255 replication but not during the entry or initiation of replication.

256 Transcriptome profiling identified mitochondrial ETC genes differentially expressed
257 upon the SOCE activation

258 The well-known SOCE-NFAT axis in Ca^{2+} signaling [31, 34] was found to be

259 independent of EV71 replication (Fig. S5). To investigate the global transcript alterations
260 upon EV71 infection alone and infection together with AnCoA4 treatment, we performed
261 RNA-seq in RD cells at 6 h p.i., a time point that AnCoA4 exerted strong antiviral activity
262 (Fig. 2C, E) and compared the differentially expressed genes. A total of 128 genes with a
263 fold change of >2 were identified (Fig. S6). Gene set enrichment analysis revealed that
264 enriched functional clusters were significantly altered in both groups. These were
265 primarily associated with the mitochondrial ETC (Table 1, Fig. 5A), which consists of four
266 complexes (CI through CIV) that couple reduction–oxidation reactions, creating an
267 electrochemical gradient that leads to the generation of ATP. The identified genes encode
268 mitochondrial NADH dehydrogenases (MT-NDs), cytochrome B (CYB), and cytochrome c
269 oxidase subunit I (COI), which belong to mitochondrial ETC CI, CIII, and CIV,
270 respectively (Table 1); in all cases, EV71 infections upregulated their RNA levels for >
271 2-fold while the infection with AnCoA4 treatment downregulated those for > 2-fold. We
272 next validated the results through RT-qPCR, which revealed a similar trend of alterations
273 in ND4, ND6, CYB, and COI transcripts following EV71 infection in the absence or
274 presence of AnCoA4 treatment (Fig. 5B). It was noted that the mitochondrial ETC RNA
275 levels from mock-infected cells upon DMSO- or AnCoA4 treatment were not altered,
276 suggesting that cells with SOCE activation are sensitive to AnCoA4 inhibition while those
277 with the basal SOCE levels are not (Fig. 5B).

278 **Disruption of SOCE reduced mitochondrial ETC RNA levels**

279 Viral 2B protein from several members of EVs causes depleted Ca^{2+} stores in the ER
280 and Golgi apparatus, resulting in an increase in cytosolic Ca^{2+}[10]. Thus, we investigated
281 the effect of EV71 2B expression alone in HeLa cells. We identified an increase in cytosolic
282 Ca^{2+} levels, which was significantly reduced by the treatment with either BAPTA, EGTA
283 or AnCoA4 (Fig. 6A). Moreover, the expression of EV71 2B alone significantly
284 upregulated the levels of ND6, CYB and COI transcripts, which were reduced by
285 AnCoA4, as did by EV71 infection in the absence or presence of SOCE inhibitor treatment
286 (Fig. 6B). Moreover, knockdown of either STIM1 or Orai1 resulted in marked reductions
287 in the mitochondrial ETC RNA levels compared with those of the scramble control in the
288 context of EV71 infection at 6 h p.i. (Fig. 6C, D); this is in agreement with those treated
289 with AnCoA4 (Fig. 5B).

290 **EV71 infection enhanced SOCE-dependent mitochondrial respiration and ATP**

291 **production**

292 Given that the upregulation of transcripts in mitochondrial ETC complexes was

293 observed during EV71 infection, we assessed several functional ETC parameters

294 (indicated in the Fig. 7A) by using a live-cell Seahorse assay [35, 36] in mock-infected cells,

295 infected cells, and infected cells treated with AnCoA4 (Fig. 7B, C). Levels of oxygen

296 consumption rate (OCR) in EV71-infected cells were increased compared to mock-infected

297 cells and reduced following AnCoA4 treatment (Fig. 7B). Concurrently, the relative levels

298 of basal and maximal respiration were also increased in EV71-infected cells and reduced

299 by AnCoA4 treatment (Fig. 7C). A similar trend of ATP production as those of the OCR

300 and basal/maximal respiration was observed (Fig. 7C). Proton leak, spare respiratory

301 capacity, and non-mitochondrial oxygen consumption remained unchanged. ETC begins

302 with CI that catalyzes electron transfer from NADH to ubiquinone, which was discovered

303 to be particularly enriched in the analysis (Table 1). We additionally investigated

304 mitochondrial CI activity upon EV71 infection with or without AnCoA4 treatment and

305 observed a marked elevation or reduction in CI activity, respectively (Fig. 7D). Given that

306 ATP is the end product of the ETC, we further determined that the cellular ATP level was

307 significantly increased following EV71 infection and reduced after AnCoA4 treatment by

308 a luminescence assay (Fig. 7E), consistent with the result analyzed by the Seahorse assay

309 (Fig. 7C). Moreover, viral RNA and protein levels decreased after treatment with

310 oligomycin, an inhibitor of mitochondrial ATP synthase (complex V) [35, 36], in a

311 dose-dependent manner (Fig. 7F, G), indicating that ATP production is essential for

312 efficient EV71 replication. Together, these results indicate that the enhancement of the

313 mitochondrial respiration was associated with increased mitochondrial CI activity and

314 bioenergy production following EV71 infection at the mid-stage (6 h p.i.), with these

315 effects likely mediated through SOCE activation.

316 **EV71 induced mitochondrial Ca^{2+} influx through SOCE**

317 EV infections cause a progressive increase in mitochondrial Ca^{2+} during infection. In
318 isolated mitochondrial systems, the addition of Ca^{2+} enhances the activities of complexes
319 I, III, and IV as well as ATP production by more than two-fold [37, 38]. Therefore, we
320 hypothesized that the upregulated levels of the complex components (Table 1 and Fig. 5A)
321 are associated with Ca^{2+} influx into mitochondria. EV71-infected cells were stained with
322 Rhod-2 AM (referred to as Rhod-2 hereafter) fluorescent dye to analyze the mitochondrial
323 Ca^{2+} levels at 6 and 12 h p.i. Depletion of ER Ca^{2+} stores by TG treatment resulted in an
324 increased level of mitochondrial Ca^{2+} compared with that in the mock control (Fig. 8A,
325 S7). The infected cells displayed progressive elevations in mitochondrial Ca^{2+} during
326 infection that were significantly decreased after treatment with ruthenium red (RR), a
327 specific inhibitor of the mitochondrial Ca^{2+} uniporter (MCU) [11, 20] that allows the
328 passage of Ca^{2+} from the cytosol into mitochondria (Fig. 8A). A similar reduction in
329 mitochondrial Ca^{2+} levels was observed following AnCoA4 addition, implying a
330 correlation of mitochondrial Ca^{2+} influx with SOCE activation. This notion was
331 supported by the finding that the expression of viral 2B alone increased mitochondrial
332 Ca^{2+} levels, which were significantly decreased following treatment with RR or AnCoA4
333 (Fig. 8B). Moreover, RR treatment reduced the ATP level promoted by EV71 infection (Fig.
334 8C), supporting the notion that elevated mitochondrial Ca^{2+} levels are associated with

335 ATP production at 6 h p.i. Next, we analyzed a panel of representative EV serotypes,

336 namely CVA16, CVB3, and Echo9, for the SOCE–mitochondrial Ca^{2+} axis at 6 h p.i. In all

337 of these serotypes, we observed that either RR- or AnCoA4 reversed mitochondrial Ca^{2+}

338 influx (Fig. 8D, F, S7), and that either treatment greatly reduced viral titers with RR

339 treatment exhibiting a dose-dependent manner (Fig. 8E, G). These findings indicate that

340 EV-induced SOCE activation facilitates viral replication through mitochondrial Ca^{2+}

341 influx and consequent ATP elevation at the mid-stage of infection (6 h p.i.).

342 **SOCE activation is correlated with cell apoptosis and virus release during the late**

343 **phase of EV71 infection**

344 EV infections induce mitochondrial Ca^{2+} overload during the late stage of the virus

345 life cycle, leading to cell death [8, 11, 20]. We investigated whether this Ca^{2+} influx results

346 in mitochondrial Ca^{2+} overload and its impact on cell fate and virus production during

347 the late phase of infection at 12 h p.i. EV71 infection markedly reduced cell viability. This

348 reduction in cell viability was reversed by AnCoA4 in a dose-dependent manner (Fig. 9A).

349 Consistent with this finding, the cell viability progressively decreased as the MOIs of the

350 virus infections increased, and all of these reductions were markedly rescued by AnCoA4

351 treatment (Fig. 9B). Because mitochondrial Ca^{2+} overload triggers apoptotic cell death, we

352 measured the caspase activities in the EV71-infected cells at 12 h p.i. after AnCoA4

353 treatment. AnCoA4 markedly reversed the EV71-induced activities of caspase -3 and -9

354 but not those of -8, indicating that the virus-induced activation of the intrinsic apoptosis

355 pathway is at least partly mediated by SOCE-mediated mitochondrial Ca^{2+} overload. We

356 next investigated whether SOCE activation and mitochondrial Ca^{2+} influx affect virus

357 production because the release of EV from cell types such as RD cells is primarily

358 mediated by apoptosis through the lytic mode [39]. AnCoA4 or RR was added to cultures

359 during EV71 infection at 0.5 MOI, and the cells and their supernatants were harvested at

360 12 h p.i. to enable measurement of the titers of intracellular (InV) and extracellular virus

361 (ExV), respectively. The ExV titer/total virus titer (E/T) ratio was determined to

362 investigate the virus release efficiency. In all cases, treatment with either AnCoA4 or RR

363 reduced the titers of ExV in a dose-dependent fashion while those of InV were not

364 reduced (Fig 9D, F). Importantly, either compound treatment resulted in dose-dependent

365 reduction in the E/T ratio (Fig. 9E, G), suggesting that blockade of the SOCE or

366 mitochondrial Ca^{2+} influx led to inhibitory effects on the viral release. Virus infection at 5

367 MOI upon AnCoA4 treatment showed a similar trend except that the E/T ratio was

368 higher than that with 0.5 MOI infection after treatment with 20 μM AnCoA4 (Fig. 9H, I).

369 Together, these findings indicate that SOCE activation and subsequent mitochondrial Ca^{2+}

370 overload play a pivotal role in the induction of apoptotic processes and facilitate the

371 egress of virus progeny at the late stage (12 h p.i.) of an infection cycle.

372 **Mouse intestinal organoids infected with EV71**

373 Given that all studies above were conducted using permissive cell lines, that is, RD
374 and HeLa cells, we investigated Ca^{2+} signal–dependent viral replication in a more
375 physiologically relevant cell culture system. We established a mouse intestinal organoid
376 culture derived from isolated intestinal stem cell–containing crypt fractions to evaluate
377 intestinal pathophysiology [22, 28, 40]. Single intestinal stem cells can be cultured into
378 three-dimensional enteroids comprising all major differentiated cell types that can be
379 found in the native intestinal organoid (Fig. 10A). However, EV infections are restricted
380 by species barriers; human cells are susceptible to such infections, whereas mouse cells
381 are typically resistant to them [41]. On the other hand, a mouse-adapted EV71 MP4 strain
382 was demonstrated to efficiently infect mouse cell cultures and a mouse model [26, 42].
383 Thus, we used a mouse-adapted EV71 MP4 strain to inoculate our mouse intestinal
384 enteroid cultures in the absence or presence of AnCoA4. Immunofluorescence staining
385 was conducted, and the levels of viral antigen were analyzed through confocal
386 microscopy. The viral antigen signals were well discernible in the infected-cells and
387 significantly reduced after AnCoA4 treatment (Fig. 10B, C). In addition, the relative levels
388 of viral RNA and representative ETC ND6, CYB and COI RNAs were analyzed. A similar
389 trend of alteration in the viral RNA was observed as those of the viral antigen (Fig. 10C,
390 D). The mouse ETC RNA levels were substantially increased following EV71 infection

391 relative to that of the mock-infected control; the levels significantly declined upon

392 treatment with AnCoA4 (Fig. 10E).

393 DISCUSSION

394 In the present study, we aimed to investigate the molecular mechanism underlying the

395 Ca^{2+} flux and its impact on the cell fate and EV life cycle. We showed that the SOCE

396 machinery likely mediated the increase in cytosolic Ca^{2+} and viral replication during the

397 mid-phase of EV71 life cycle (Fig. 1–4). Moreover, we demonstrated that the ETC complex

398 genes were enriched through SOCE during the mid-stage of infection (Table 1, Fig 5A).

399 This resulted in alterations in the mitochondrial ETC CI activity, ATP production and

400 cellular respiration (Fig. 5, 6, 7) through SOCE and mitochondrial Ca^{2+} influx, and

401 contributed to viral replication (Fig. 6, 8). The SOCE–mitochondrial Ca^{2+} influx axis also

402 plays a role, at least in part, in triggering apoptosis and subsequent viral release due to

403 mitochondrial Ca^{2+} overload during the late stage of virus infection (Fig. 9).

404 We started with investigating the potential contribution of the enhanced cytosolic Ca^{2+}

405 to different stages of the viral life cycle. It was demonstrated that regardless of the

406 infection doses, EV71 replication upon the treatments of BAPTA, EGTA or AnCoA4

407 showed the delay kinetics relative to that of untreated control, with the delay most
408 pronounced at 4 h and 6 h p.i. (Fig. 1B, 1D, 2C, 2E, S3). This is consistent with the finding
409 that AnCoA4 treatment between 3-6 h after viral adsorption, but not other periods
410 assessed, resulted in a reduced viral titer (Fig. 2F, G). It is speculated that viral-enhanced
411 mitochondrial function and ATP production facilitate virus replication during the
412 mid-stage of replication. Once the infection passes the virus replication stage highly
413 required for ATP and proceeds to 9 h and 12 h p.i., the differences in viral titers between
414 the AnCoA4-treated and DMSO control groups significantly decreased (Fig. 2C, E).
415 Nevertheless, virus release was significantly impaired regardless of the inoculated virus
416 doses at 12 h p.i., likely due to inhibition of the mitochondrial Ca^{2+} overload and the
417 consequent proapoptotic state by AnCoA4 (Fig. 9H, I). Indeed, these data are in
418 agreement with the report that recombinant coxsackievirus B3 carrying the mutant 2B also
419 exhibited a delay in viral replication at the earlier stage and a defect in virus release and
420 that virus release was greatly hampered when the infected cells were cultured in the
421 Ca^{2+}-free medium compared with that in the Ca^{2+}-containing medium [10]. This
422 proposed mechanism (Fig. 11) is supported by our finding that the expression of EV71 2B
423 alone resulted in SOCE-dependent increases in the ETC transcripts and mitochondrial
424 Ca^{2+} levels (Fig 6B, 8B).

425 Individual expression of EV 2B is known to induce the influx of extracellular Ca^{2+};

426 however, the precise mechanism has not been defined [7, 10]. In this study, we clearly
427 showed that knockdown of either STIM1 or Orai1 resulted in reduced levels of the
428 virus-induced cytosolic Ca^{2+} and mitochondrial ETC RNA as well as those of viral protein
429 and viral titers (Fig. 3A-C, Fig. 6C, D). These data indicate that the STIM1-Orai1
430 machinery contributes to the extracellular Ca^{2+} influx into the cytosol during EV infection,
431 consistent with the effects caused by AnCoA4 treatments (Fig. 2, 5). The STIM1–Orai1
432 machinery has been reported to mediate the replication of some viruses. The activation of
433 the STIM1 and Orai1 channels promotes virion assembly and budding during Ebola or
434 Marburg virus infection [43]. The replication capacity of certain viruses, such as dengue
435 virus and rotavirus [44, 45], relies on Ca^{2+} influx through the STIM1–Orai1 system. The
436 hepatitis B virus HBx protein directly binds to and modifies STIM1–Orai1 complexes,
437 regulating Ca^{2+} levels and thereby promoting viral replication by modulating
438 mitochondrial Ca^{2+} uptake [46]. However, the downstream signaling pathways
439 responsible for their replication remain unknown. Some viruses inactivate SOCE to
440 reduce immune responses and facilitate viral replication. For example, a study reported
441 that the downregulation of type I interferon through Orai1 depletion facilitated
442 SARS-CoV-2 infection [47]. In the current study, we determined that SOCE participates in
443 two steps of the virus life cycle, namely viral replication and virion release, through
444 progressive mitochondrial Ca^{2+} influx. This represents a novel mechanism involving

445 SOCE-mediated virus replication.

446 The findings of our RNA-seq/bioinformatic analysis revealed that a panel of
447 components of mitochondrial ETC complexes were enriched. Because the primary
448 function of mitochondria is to generate ATP through oxidative phosphorylation, we
449 investigated the function correlations between these components and determined that
450 EV71 infection increased mitochondrial ETC CI activity, ATP levels, and cellular
451 respiration. These effects were significantly attenuated following the blockade of SOCE or
452 mitochondrial Ca^{2+} influx by AnCoA4 or RR, respectively. These findings are consistent
453 with those of previous studies indicating that a moderate increase in mitochondrial Ca^{2+}
454 promotes the activities of the ETC CI, CIII, and CIV as well as ATP production [37, 38, 48].
455 Regarding the role of increased ATP in EV replication, studies have demonstrated that EV
456 2C plays a crucial role in virus replication by acting as an ATP-dependent RNA helicase
457 for virus RNA replication. Moreover, EV71 infection induces mitochondrial clustering
458 and recruitment, suggesting localized ATP production occurs at the virus replication site.
459 Prior to this study, some viruses, including cytomegalovirus, dengue virus, and vaccinia

460 virus, have been reported to promote mitochondrial ETC function and subsequent energy
461 output to support virus replication [35, 36, 49]. Although the mechanisms underlying this
462 phenomenon remain largely unknown for dengue virus and vaccinia virus, the
463 cytomegalovirus protein pUL13 has been demonstrated to interact with mitochondrial
464 cristae to enhance ETC function [36]. On the other hand, some other viruses undergo their
465 replication without upregulating ETC activity. This is best known for hepatitis C virus
466 and influenza viruses whose ATP-dependent replication mainly rely on the glycolysis
467 pathways rather than ETC activity [50, 51, 52]. This is in marked contrast to our RNA-seq
468 analysis where the mitochondrial ETC transcripts, but not those in the glycolysis
469 pathways, were enriched (Table 1, Fig S6). To the best of our knowledge, this is the first
470 study to report that EV71 infection augments ETC activity and ATP production to support
471 virus replication and that it employs distinct mechanisms involving SOCE activation and
472 mitochondrial Ca^{2+} influx.

473 Studies on a diverse group of viruses, including EVs, have revealed that viruses
474 induce substantial and persistent increases in mitochondrial Ca^{2+} levels, leading to
475 apoptotic cell death, especially during the late stages of the infection cycle. In addition to
476 being localized in the ER, the EV71 2B protein was demonstrated to localize to
477 mitochondria, thereby directly binding to and activating the proapoptotic protein Bax [53].
478 This interaction ensures the induction of cell apoptosis, potentially exacerbating the

479 intrinsic apoptosis driven by mitochondrial Ca^{2+} overload, as demonstrated in this study.
480 Other mechanisms, including EV71-induced, caspase-independent activation of the
481 apoptosis-inducing factor, may contribute to apoptosis, maximizing cell death and virus
482 release.

483 Human intestinal organoid models have been established and used to study EVs,
484 including EV71 [54, 55, 56]. In this study, we used a mouse intestinal organoid culture
485 system developed from an inbred mouse origin (Fig. 10A). This system offers a stable,
486 homogenous and continuous supply of organoids [22, 28, 40], whereas a human model
487 does not [57]. Compared with infections by human EV71 strain without
488 mouse-adaptation, the use of a mouse-adapted MP4 strain greatly enhanced the infection
489 efficiency in mice [26, 42] and in the mouse intestinal organoid culture (our unpublished
490 data). We used the mouse-adapted EV71 strain MP4 for infection, and viral antigen was
491 well discernible in the mouse intestinal organoids in a SOCE-dependent manner (Fig. 10B,
492 C). This is consistent with the report that SOCE activation could be demonstrated in a
493 human intestinal organoid culture [58]. In addition, we observed a concurrent increase in
494 the levels of mouse ETC ND6, CYB and COI transcripts along with EV71 RNA, all in a
495 SOCE-dependent manner (Fig. 10D, E). These findings indicate that our mouse intestinal
496 organoid system provides a valuable and physiologically relevant platform for in-depth
497 study of virus-induced alterations in host Ca2+ signaling.

498 Our study demonstrated that the SOCE- and mitochondrial Ca^{2+} influx-dependent

499 virus replication can be recapitulated with infections involving other representative EV

500 serotypes (Fig. 8E, G). This led us to speculate whether spatial and temporal control of

501 Ca2+ signals, as observed in EV infections, is a common manifestation in viral replication.

502 If this speculation is confirmed, host channels that support these Ca2+ signals, such as

503 STIM1 and Orai1, may represent novel targets for the development of broadly effective

504 host-directed antiviral therapeutics.

505 ACKNOWLEDGMENTS

506 This study was supported in part by the Professor Tsuei-Chu Mong Merit Scholarship

507 (grant 40719001), NYMU-FEMH Joint Research Program (grant 110DN40), and the

508 Ministry of Science and Technology, Taiwan, ROC (111-2320-B-A49-026-).

509 Supplemental material

510 1. Supplemental material and method

511 2. Supplemental table

512 3. supplemental figures

514 # REFERENCES

515 ## References

516 [1] **Baggen J, Thibaut HJ, Strating J, van Kuppeveld FJM**. 2018. The life cycle of

517 non-polio enteroviruses and how to target it. *Nat Rev Microbiol* 16 (6):368–381.

518 [2] **Liu SL, Pan H, Liu P, Amer S, Chan TC, Zhan J, Huo X, Liu Y, Teng Z, Wang L,**

519 **Zhuang H**. 2015. Comparative epidemiology and virology of fatal and nonfatal cases

520 of hand, foot and mouth disease in mainland China from 2008 to 2014. *Rev Med Virol*

521 25 (2):115–28.

522 [3] **Chami M, Oules B, Paterlini-Brechot P**. 2006. Cytobiological consequences of

523 calcium-signaling alterations induced by human viral proteins. *Biochim Biophys Acta*

524 1763 (11):1344–62.

525 [4] **Zhou Y, Frey TK, Yang JJ**. 2009. Viral calciomics: interplays between Ca2+ and virus.

526 *Cell Calcium* 46 (1):1–17.

527 [5] **Aldabe R, Irurzun A, Carrasco L**. 1997. Poliovirus protein 2BC increases cytosolic free

528 calcium concentrations. *J Virol* 71 (8):6214–7.

529 [6] **Bozym RA, Morosky SA, Kim KS, Cherry S, Coyne CB**. 2010. Release of intracellular
530 calcium stores facilitates coxsackievirus entry into polarized endothelial cells. *PLoS*
531 *Pathog* 6 (10):e1001135.

532 [7] **Campanella M, de Jong AS, Lanke KW, Melchers WJ, Willems PH, Pinton P,**
533 **Rizzuto R, van Kuppeveld FJ**. 2004. The coxsackievirus 2B protein suppresses
534 apoptotic host cell responses by manipulating intracellular Ca2+ homeostasis. *J Biol*
535 *Chem* 279 (18):18440–50.

536 [8] **van Kuppeveld FJ, van den Hurk PJ, van der Vliet W, Galama JM, Melchers WJ**.
537 1997. Chimeric coxsackie B3 virus genomes that express hybrid
538 coxsackievirus-poliovirus 2B proteins: functional dissection of structural domains
539 involved in RNA replication. *J Gen Virol* 78 (Pt 8):1833–40.

540 [9] **van Kuppeveld FJ, de Jong AS, Melchers WJ, Willems PH**. 2005. Enterovirus protein
541 2B po(u)res out the calcium: a viral strategy to survive? *Trends Microbiol* 13 (2):41–4.

542 [10] **van Kuppeveld FJ, Hoenderop JG, Smeets RL, Willems PH, Dijkman HB, Galama**
543 **JM, Melchers WJ**. 1997. Coxsackievirus protein 2B modifies endoplasmic reticulum
544 membrane and plasma membrane permeability and facilitates virus release. *EMBO J*
545 16 (12):3519–32.

546 [11] **Brisac C, Téoulé F, Autret A, Pelletier I, Colbère-Garapin F, Brenner C, Lemaire C,**
547 **Blondel B**. 2010. Calcium flux between the endoplasmic reticulum and mitochondrion
548 contributes to poliovirus-induced apoptosis. *J Virol* 84 (23):12226–35.

549 [12] **Ao D, Sun SQ, Guo HC**. 2014. Topology and biological function of enterovirus
550 non-structural protein 2B as a member of the viroporin family. *Vet Res* 45:87.

551 [13] **Nieva JL, Madan V, Carrasco L**. 2012. Viroporins: structure and biological functions.
552 *Nat Rev Microbiol* 10 (8):563–74.

553 [14] **Nieto-Torres JL, Verdia-Baguena C, Castano-Rodriguez C, Aguilella VM, Enjuanes**
554 **L**. 2015. Relevance of Viroporin Ion Channel Activity on Viral Replication and
555 Pathogenesis. *Viruses* 7 (7):3552–73.

556 [15] **van Kuppeveld FJ, Galama JM, Zoll J, van den Hurk PJ, Melchers WJ**. 1996.
557 Coxsackie B3 virus protein 2B contains cationic amphipathic helix that is required for
558 viral RNA replication. *J Virol* 70 (6):3876–86.

559 [16] **Soboloff J, Rothberg BS, Madesh M, Gill DL**. 2012. STIM proteins: dynamic
560 calcium signal transducers. *Nat Rev Mol Cell Biol* 13 (9):549–65.

561 [17] **Hogan PG, Lewis RS, Rao A**. 2010. Molecular basis of calcium signaling in
562 lymphocytes: STIM and ORAI. *Annu Rev Immunol* 28:491–533.

563 [18] **Takemura H, Hughes AR, Thastrup O, Putney J J W**. 1989. Activation of calcium
564 entry by the tumor promoter thapsigargin in parotid acinar cells. Evidence that an
565 intracellular calcium pool and not an inositol phosphate regulates calcium fluxes at
566 the plasma membrane. *J Biol Chem* 264 (21):12266–71.

567 [19] **Shaw PJ, Feske S**. 2012. Regulation of lymphocyte function by ORAI and STIM
568 proteins in infection and autoimmunity. *J Physiol* 590 (17):4157–67.

569 [20] **Lu JR, Lu WW, Lai JZ, Tsai FL, Wu SH, Lin CW, Kung SH**. 2013. Calcium flux and
570 calpain-mediated activation of the apoptosis-inducing factor contribute to enterovirus
571 71-induced apoptosis. *J Gen Virol* 94 (Pt 7):1477–85.

572 [21] **Supasorn O, Tongtawe P, Srimanote P, Rattanakomol P, Thanongsaksrikul J**. 2020.
573 A nonstructural 2B protein of enterovirus A71 increases cytosolic Ca(2+) and induces
574 apoptosis in human neuroblastoma SH-SY5Y cells. *J Neurovirol* 26 (2):201–213.

575 [22] **Chen Y, Lee SH, Tsai YH, Tseng SH**. 2014. Ischemic preconditioning increased the
576 intestinal stem cell activities in the intestinal crypts in mice. *J Surg Res* 187 (1):85–93.

577 [23] **Zietek T, Rath E, Haller D, Daniel H**. 2015. Intestinal organoids for assessing
578 nutrient transport, sensing and incretin secretion. *Sci Rep* 5:16831.

579 [24] **Ludikhuize MC, Meerlo M, Gallego MP, Xanthakis D, Burgaya Julià M, Nguyen**
580 **NTB, Brombacher EC, Liv N, Maurice MM, Paik JH, Burgering BMT,**
581 **Rodriguez Colman MJ**. 2020. Mitochondria Define Intestinal Stem Cell Differentiation
582 Downstream of a FOXO/Notch Axis. *Cell Metab* 32 (5):889–900.e7.

583 [25] **Tseng KC, Hsu BY, Ling P, Lu WW, Lin CW, Kung SH**. 2022. Antidepressant
584 Sertraline Is a Broad-Spectrum Inhibitor of Enteroviruses Targeting Viral Entry
585 through Neutralization of Endolysosomal Acidification. *Viruses* 14 (1).

586 [26] **Wang YF, Chou CT, Lei HY, Liu CC, Wang SM, Yan JJ, Su IJ, Wang JR, Yeh TM,**
587 **Chen SH, Yu CK**. 2004. A mouse-adapted enterovirus 71 strain causes neurological
588 disease in mice after oral infection. *J Virol* 78 (15):7916–24.

589 [27] **Huang DW, Sherman BT, Tan Q, Kir J, Liu D, Bryant D, Guo Y, Stephens R, Baseler**
590 **MW, Lane HC, Lempicki RA**. 2007. DAVID Bioinformatics Resources: expanded
591 annotation database and novel algorithms to better extract biology from large gene
592 lists. *Nucleic Acids Res* 35 (Web Server issue):W169–75.

593 [28] **Chen Y, Li C, Tsai YH, Tseng SH**. 2019. Intestinal Crypt Organoid: Isolation of
594 Intestinal Stem Cells, In Vitro Culture, and Optical Observation. *Methods Mol Biol*
595 1576:215–228.

596 [29] **Cui C, Merritt R, Fu L, Pan Z**. 2017. Targeting calcium signaling in cancer therapy.
597 *Acta Pharm Sin B* 7 (1):3–17.

598 [30] **Yuan J, Shen L, Wu J, Zou X, Gu J, Chen J, Mao L**. 2018. Enterovirus A71 Proteins:
599 Structure and Function. *Front Microbiol* 9:286.

600 [31] **Sadaghiani AM, Lee SM, Odegaard JI, Leveson-Gower DB, McPherson OM,**
601 **Novick P, Kim MR, Koehler AN, Negrin R, Dolmetsch RE, Park CY**. 2014.
602 Identification of Orai1 channel inhibitors by using minimal functional domains to
603 screen small molecule microarrays. *Chem Biol* 21 (10):1278–1292.

604 [32] **Antigny F, Jousset H, König S, Frieden M**. 2011. Thapsigargin activates Ca^2+ entry
605 both by store-dependent, STIM1/Orai1-mediated, and store-independent,
606 TRPC3/PLC/PKC-mediated pathways in human endothelial cells. *Cell Calcium* 49
607 (2):115–27.

608 [33] **Manders EMM, Verbeek FJ, Aten JA**. 1993. Measurement of co-localization of

609 objects in dual-colour confocal images. *J Microsc* 169 (3):375–382.

610 [34] **Vaeth M, Maus M, Klein-Hessling S, Freinkman E, Yang J, Eckstein M, Cameron S,**
611 **Turvey SE, Serfling E, Berberich-Siebelt F, Possemato R, Feske S**. 2017.
612 Store-Operated Ca(2+) Entry Controls Clonal Expansion of T Cells through Metabolic
613 Reprogramming. *Immunity* 47 (4):664–679.e6.

614 [35] **Barbier V, Lang D, Valois S, Rothman AL, Medin CL**. 2017. Dengue virus induces
615 mitochondrial elongation through impairment of Drp1-triggered mitochondrial
616 fission. *Virology* 500:149–160.

617 [36] **Betsinger CN, Jankowski CSR, Hofstadter WA, Federspiel JD, Otter CJ,**
618 **Jean Beltran PM, Cristea IM**. 2021. The human cytomegalovirus protein pUL13
619 targets mitochondrial cristae architecture to increase cellular respiration during
620 infection. *Proc Natl Acad Sci U S A* 118 (32).

621 [37] **Glancy B, Willis WT, Chess DJ, Balaban RS**. 2013. Effect of calcium on the oxidative
622 phosphorylation cascade in skeletal muscle mitochondria. *Biochemistry* 52
623 (16):2793–809.

624 [38] **Territo PR, French SA, Dunleavy MC, Evans FJ, Balaban RS**. 2001. Calcium
625 activation of heart mitochondrial oxidative phosphorylation: rapid kinetics of mVO2,
626 NADH, AND light scattering. *J Biol Chem* 276 (4):2586–99.

627 [39] **Owusu IA, Quaye O, Passalacqua KD, Wobus CE**. 2021. Egress of non-enveloped
628 enteric RNA viruses. *J Gen Virol* 102 (3).

629 [40] **Chen Y, Tsai YH, Tseng BJ, Tseng SH**. 2019. Influence of Growth Hormone and
630 Glutamine on Intestinal Stem Cells: A Narrative Review. *Nutrients* 11 (8).

631 [41] **Yamayoshi S, Yamashita Y, Li J, Hanagata N, Minowa T, Takemura T, Koike S**. 2009.
632 Scavenger receptor B2 is a cellular receptor for enterovirus 71. *Nature Medicine* 15
633 (7):798–801.

634 [42] **Huang HI, Lin JY, Chen HH, Yeh SB, Kuo RL, Weng KF, Shih SR**. 2014. Enterovirus
635 71 infects brain-derived neural progenitor cells. *Virology* 468-470:592–600.

636 [43] **Han Z, Madara JJ, Herbert A, Prugar LI, Ruthel G, Lu J, Liu Y, Liu W, Liu X, Wrobel**

637 **JE, Reitz AB, Dye JM, Harty RN, Freedman BD**. 2015. Calcium Regulation of
638 Hemorrhagic Fever Virus Budding: Mechanistic Implications for Host-Oriented
639 Therapeutic Intervention. *PLoS Pathog* 11 (10):e1005220.

640 [44] **Hyser JM, Utama B, Crawford SE, Broughman JR, Estes MK**. 2013. Activation of the
641 endoplasmic reticulum calcium sensor STIM1 and store-operated calcium entry by
642 rotavirus requires NSP4 viroporin activity. *J Virol* 87 (24):13579–88.

643 [45] **Dionicio CL, Pena F, Constantino-Jonapa LA, Vazquez C, Yocupicio-Monroy M,**
644 **Rosales R, Zambrano JL, Ruiz MC, Del Angel RM, Ludert JE**. 2018. Dengue virus
645 induced changes in Ca(2+) homeostasis in human hepatic cells that favor the viral
646 replicative cycle. *Virus Res* 245:17–28.

647 [46] **Yao JH, Liu ZJ, Yi JH, Wang J, Liu YN**. 2018. Hepatitis B Virus X Protein Upregulates
648 Intracellular Calcium Signaling by Binding C-terminal of Orail Protein. *Curr Med Sci*
649 38 (1):26–34.

650 [47] **Wu B, Ramaiah A, Garcia J G, Hasiakos S, Arumugaswami V, Srikanth S**. 2022.
651 ORAI1 Limits SARS-CoV-2 Infection by Regulating Tonic Type I IFN Signaling. *J*
652 *Immunol* 208 (1):74–84.

653 [48] **Di Benedetto G, Scalzotto E, Mongillo M, Pozzan T**. 2013. Mitochondrial Ca(2)(+)
654 uptake induces cyclic AMP generation in the matrix and modulates organelle ATP
655 levels. *Cell Metab* 17 (6):965–975.

656 [49] **Chang CW, Li HC, Hsu CF, Chang CY, Lo SY**. 2009. Increased ATP generation in the
657 host cell is required for efficient vaccinia virus production. *J Biomed Sci* 16 (1):80.

658 [50] **Gerresheim GK, Bathke J, Michel AM, Andreev DE, Shalamova LA, Rossbach O,**
659 **Hu P, Glebe D, Fricke M, Marz M, Goesmann A, Kiniry SJ, Baranov PV, Shatsky IN,**
660 **Niepmann M**. 2019. Cellular Gene Expression during Hepatitis C Virus Replication as
661 Revealed by Ribosome Profiling. *Int J Mol Sci* 20 (6).

662 [51] **Perrin-Cocon L, Kundlacz C, Jacquemin C, Hanoulle X, Aublin-Gex A, Figl M,**

663 **Manteca J, André P, Vidalain PO, Lotteau V, Diaz O**. 2022. Domain 2 of Hepatitis C
664 Virus Protein NS5A Activates Glucokinase and Induces Lipogenesis in Hepatocytes.
665 *Int J Mol Sci* 23 (2).

666 [52] **Keshavarz M, Solaymani-Mohammadi F, Namdari H, Arjeini Y, Mousavi MJ,**
667 **Rezaei F**. 2020. Metabolic host response and therapeutic approaches to influenza
668 infection. *Cell Mol Biol Lett* 25:15.

669 [53] **Cong H, Du N, Yang Y, Song L, Zhang W, Tien P**. 2016. Enterovirus 71 2B Induces
670 Cell Apoptosis by Directly Inducing the Conformational Activation of the
671 Proapoptotic Protein Bax. *J Virol* 90 (21):9862–9877.

672 [54] **Good C, Wells AI, Coyne CB**. 2019. Type III interferon signaling restricts enterovirus
673 71 infection of goblet cells. *Sci Adv* 5 (3):eaau4255.

674 [55] **Zhao X, Li C, Liu X, Chiu MC, Wang D, Wei Y, Chu H, Cai JP, Hau-Yee Chan I,**
675 **Kak-Yuen Wong K, Fuk-Woo Chan J, Kai-Wang To K, Yuen KY, Zhou J**. 2021.
676 Human Intestinal Organoids Recapitulate Enteric Infections of Enterovirus and
677 Coronavirus. *Stem Cell Reports* 16 (3):493–504.

678 [56] **Drummond CG, Bolock AM, Ma C, Luke CJ, Good M, Coyne CB**. 2017.
679 Enteroviruses infect human enteroids and induce antiviral signaling in a cell
680 lineage-specific manner. *Proc Natl Acad Sci U S A* 114 (7):1672–1677.

681 [57] **Kim J, Koo BK, Knoblich JA**. 2020. Human organoids: model systems for human
682 biology and medicine. *Nat Rev Mol Cell Biol* 21 (10):571–584.

683 [58] **Chang-Graham AL, Perry JL, Strtak AC, Ramachandran NK, Criglar JM, Philip**
684 **AA, Patton JT, Estes MK, Hyser JM**. 2019. Rotavirus Calcium Dysregulation
685 Manifests as Dynamic Calcium Signaling in the Cytoplasm and Endoplasmic
686 Reticulum. *Sci Rep* 9 (1):10822.

687 **FIGURE LEGEND**

FIG 1 EV71 infection induced elevated cytosolic Ca^{2+} levels that correlated

with the progression of viral replication. RD cells were mock-infected (M) or infected with EV71 stock at an MOI of 0.5 (A, B) or 5 (C, D) for the indicated times in the presence of BAPTA (10 μM), EGTA (1.8 mM), or DMSO control. (A, C) Cells were stained with Fluo-8 for 30 mins. Fluorescence intensities were quantified relative to the mock-infected controls. (B, D) Cell lysates and supernatants were collected at the indicated times. Total virus titers were determined by $TCID_{50}$ assay (See Text S1). Data represent mean values from experiments conducted in triplicate, with error bars indicating standard deviations (SDs). ***$p < 0.001$, **$p < 0.01$, *$p < 0.05$ versus the DMSO control.

FIG 2 A specific SOCE blocker AnCoA4 reduced virus-induced cytosolic Ca^{2+} levels and viral replication. (A) RD cells were infected with EV71 at an MOI of 0.5 for 6 h in the presence of DMSO control or 10 and 20 μM AnCoA4. RD cells were mock-infected (M) or infected with EV71 stock at an MOI of 0.5 (B, C) or 5 (D, E) for the indicated times in the presence of 20 μM AnCoA4 or DMSO control. (B, D) Cells were stained with Fluo-8 for 30 mins. Fluorescence intensities were quantified relative to the mock-infected controls. (C, E) Cell lysates and supernatants were collected at the indicated time. Total virus titers were determined by $TCID_{50}$ assay. (F) Timing of EV71 inhibition by AnCoA4 with the schematic representation. AnCoA4 was added to RD cells at the indicated times relative to viral infection at an MOI of 0.5, with the initiation (0 h) and completion (1 h) of viral adsorption indicated. The bars indicate the periods with AnCoA4 treatment. Viral supernatants and cell lysates were collected at the end of 6 h for all treatment conditions. (I) Whole: -1 to 6 h; (II) entry: -1 to 1 h; (III)

early: 1–3 h; (IV) viral replication: 3-6 h. (G) Total virus titers were determined by $TCID_{50}$ assay. Data represent mean values from experiments conducted in triplicate, with error bars indicating standard deviations (SDs). ***$p < 0.001$, **$p < 0.01$, *$p < 0.05$ versus the DMSO control.

FIG 3 Both Orai1 and STIM1 are essential during active replication of EV71. HeLa cells were transduced with lentivirus–shScramble, –shOrai1 or –shSTIM1 48 h prior to infection with EV71 at 0.5 MOI for 6 h and 12 h. (A) Cells were stained with Fluo-8 for cytosolic Ca^{2+} measurement. (B) Cell lysates were harvested and levels of viral VP1 protein and tubulin (the internal control) were measured by immunoblot analysis. The percentage shown below each lane represents the intensity of viral VP1 relative to that of tubulin. (C) Total virus titers were determined by $TCID_{50}$. The experiments were conducted in triplicate, and shown as means ± SDs. ***$p < 0.001$,**$p < 0.01$, *$p < 0.05$ versus the scramble control.

FIG 4 EV71 infection and viral 2B expression induced enhanced colocalization of STIM1 and Orai1. (A) HeLa-STIM1-Orai1 cells coexpressing EGFP–STIM1 (green) and mOrange–Orai1 (red) were mock-infected or infected with EV71 at an MOI of 1 for 9 h in the absence or presence of AnCoA4 at 20 μM. Treatment with 5 μM thapsigargin for 15 mins served as a positive control for SOCE activation. (B) HeLa-STIM1-Orai1 cells were also transfected with pCMV-Flag-2B (2B) plasmid for 48 h. EV71 VP1 (A) or 2B (B) was detected using the anti-EV71 primary Ab or anti-Flag Ab, respectively, followed by the

Cy5-labeled secondary antibody (blue) . Colocalization of EGFP–STIM1 and mOrange-Orai1 is presented in yellow. Cell nuclei were stained with DAPI (white). (C, D) The colocalization between EGFP–STIM1 and mOrange-Orai1 was measured using Mander's coefficients. Each bar represents the mean Mander's coefficient for a specific experimental condition, reflecting the degree of colocalization between Orai1 and STIM1. Images were acquired using a Zeiss LSM880 confocal microscope. The scale bar represents 5 μM. ***$p < 0.001$,**$p < 0.01$, *$p < 0.05$ versus the mock-infected or EV71-infected group.

FIG 5 Transcriptome profiling identified mitochondrial ETC genes differentially expressed during EV71 infection.(A) Heatmap of differentially expressed genes between the DMSO- and AnCoA4-treated groups, both in the context of EV71 infection at an MOI of 0.5 for 6 h in RD cells. The numbers for each gene indicated the change folds. (B) RD cells were infected with EV71 at an MOI of 0.5 for 6 h or mock infected. The mock-infected cells or EV-infected were treated with 20 μM AnCoA4 or DMSO. Relative RNA levels of representative components of ETC complexes, as indicated, were determined through RT-qPCR by using total RNA prepared under each condition and shown as levels relative to those of mock-infected controls. RNA level was normalized with internal control GAPDH. ***$p < 0.001$,**$p < 0.01$, *$p < 0.05$ versus the DMSO control or EV71-infected group.

FIG 6 2B expression and EV71 infection induced transcriptional upregulation of mitochondrial ETC genes through SOCE machinery. (A) HeLa cells were

transfected with pFLAG-CMV-2 (empty) plasmid, pCMV-FLAG-2B (2B) plasmid, or left untransfected (Unt) for 40 h. For untransfected and empty controls, media were replaced with DMSO-containing media, and incubated for 8 h. For the pCMV-FLAG-2B -transfected cells, media were replaced with DMSO-, 10 μM BAPTA-, 1.8 mM EGTA- ,or 20 μM AnCoA4-containing medium, as indicated, and also incubated for 8 h. Cells were stained with the cytosolic Ca^{2+} fluorescent dye Fluo-8. (B) HeLa cells were transfected with the empty or 2B-expressing plasmids for 48 h. HeLa cells with knockdown of STIM1 (C) or Orai1 (D), each with Scramble control, were infected with EV71 at an MOI of 0.5 for 6h. Relative RNA levels of representative components of ETC complexes, as indicated, were determined through RT-qPCR. The expression levels were related to those of mock-infected scramble controls. ***$p < 0.001$,**$p < 0.01$, *$p < 0.05$ versus the mock-infected or DMSO control.

FIG 7 EV71-infected cells displayed increased mitochondrial respiration and ATP production through the SOCE machinery. (A) Diagram illustrating the oxygen consumption rate (OCR) measured for the parameters including basal respiration, maximal respiration, proton leak, ATP production, spare respiratory capacity, and non-mitochondrial oxygen consumption of ETC function, by using the XFe24 Seahorse analyzer; this diagram was reproduced with permission. (B) HeLa cells were mock-infected or infected with EV71 (MOI = 5) for 6 h in the absence or presence of AnCoA4 at 20 μM. Oligomycin, FCCP, and antimycin A + rotenone were injected at the times indicated in (A). (C) The six parameters were analyzed following the manufacturer's instructions and are presented as percentages relative to the mock-infected cells. (D) Mitochondria were isolated from HeLa cells for the complex I activity assay and shown as levels relative to those of mock-infected controls. (E) Cellular ATP activity was measured by a luminescence assay and reported as levels relative to those of mock-infected controls. (F, G) HeLa cells were infected with EV71 at an MOI of 0.5 with oligomycin treated at the indicated concentrations or DMSO control. Total RNA and cell lysates were collected at 6 h p.i. for RT-qPCR (F) and immunoblots (G) , respectively. Relative RNA level was normalized with internal control GAPDH. The percentage shown below each lane represents the intensity of viral VP1 relative to that of GAPDH. Data are presented as means ± SDs. ***$p < 0.001$,**$p < 0.01$, *$p < 0.05$ versus the mock-infected or EV71-infected groups.

FIG 8 EV71 infections increased the mitochondrial Ca^{2+} influx that contributed to viral replication and ATP production at the mid-stage of the virus life cycle.

(A) HeLa cells were treated with 10 μM RR, 20 μM AnCoA4, or DMSO control during EV71 infection at an MOI of 0.5 for 6 h and 12 h and were then stained with Rhod-2. TG served as a positive control for Rhod-2 stain. The relative Rhod-2 fluorescence intensity of each condition was quantified relative to that of a mock-infected control (M), and normalized by the number of cells stained with DAPI. (B) HeLa cells were transfected with an empty or 2B-expressing plasmid for 40 h. The media were replaced with DMSO, 10 μM RR, or 20 μM AnCoA4-containing media for 8 h and then stained with Rhod-2. (C) HeLa cells were infected with EV71 at an MOI of 5 for 6 h or mock-infected and treated with 10 μM RR or DMSO. Cellular ATP activity was measured and reported as levels relative to those of the mock-infected control. HeLa cells were infected with EV71, CVA16, CVB3, or Echo 30, each at an MOI of 1 for 6 h and were treated with 20 μM AnCoA4 (D, E), 10/20 μM RR (F, G), each with DMSO control, during the infection period. (D, F) Cells were stained for Rhod-2 or (E, G) total virus titer was determined by $TCID_{50}$ assay and shown as the percentage of their DMSO controls. The experiments were conducted in triplicate, and their means ± SDs are presented. ***$p < 0.001$,**$p < 0.01$, *$p < 0.05$ versus the mock-infected or DMSO control.

FIG 9 The SOCE inhibitor AnCoA4 attenuated EV71-induced apoptosis and the viral release at the late stage of infection. (A) RD cells were mock-infected or infected with EV71 at an MOI of 5 for 12 h. The infected cells were treated with the indicated concentrations of AnCoA4 or DMSO control. (B) EV71 was used to infect RD cells at MOIs of 1, 2, and 5 for 12 h, and cells were treated with 10 μM

AnCoA4 or DMSO control. Cell viability was measured using the MTS assay and compared with that of mock-infected controls . (C) RD cells were mock-infected or infected with EV71 at an MOI of 1 for 12 h and treated with 20 μM AnCoA4 during infection or DMSO control. Caspase-3, -8, and -9 activities were measured using the caspase fluorometric assays. RD cells were infected with EV71 at an MOI of 0.5 for 12 h and treated with AnCoA4 (D) or RR (F), both at 10- and 20-μM, during the infection period. At 12 h p.i., the supernatant was collected for the extracellular virus (ExV), and cells were trypsinized for preparing the intracellular virus (InV). The titers of ExVs and InVs in each group were determined using the $TCID_{50}$ assay (D, F). For each condition, the relative ratio of the ExV titer over the total virus titer, compared with that of untreated control, is represented by the E/T ratio (%). (H) RD cells were infected with EV71 at an MOI of 5 for 12 h and treated with AnCoA4 at 10- and 20-μM. At 12 h p.i., the supernatant was collected for the extracellular virus (ExV), and intracellular virus (InV). The titers of ExVs and InVs in each group were determined using the $TCID_{50}$ assay (D, F, H). For each condition, the relative ratio of the ExV titer over the total virus titer, compared with that of untreated control, is represented by the E/T ratio (%) (E, G, I) and indicates the virus release efficiency. Data represented the means of triplicated experiments and the SD Data represented the means of triplicated experiments and the SD. ***$p < 0.001$,**$p < 0.01$, *$p < 0.05$ versus the DMSO control.

FIG 10 EV71 replication and virus-upregulated ETC RNA were reduced by AnCoA4 in the mouse intestinal organoid model. (A) Schematic representation

of the three-dimensional mouse intestinal organoid culture. (B) Mouse intestinal organoid cultures seeded in Xfe 24-well dishes were inoculated with 200μl EV71 MP4 strain (4×10^8 $TCID_{50}$/mL) for 48 h and treated with 20μM AnCoA4 during the infection period or DMSO control. Immunofluorescence assay was conducted, with viral VP1 antigen detected using the mouse anti-EV71 Ab (green) and the nucleus stained with DAPI (blue). (C) The relative VP1 positive (+) antigen expression of MP4-infected, DMSO-treated, and MP4 infected, AnCoA4-treated cells were quantified relative to the number of cells stained with DAPI. Total RNA was prepared, and viral RNA (D) and the indicated mitochondrial ETC RNA (E) were measured through RT-qPCR and presented as levels relative to those of the mock-infected controls (%). Data are presented as means ± SDs. ***$p < 0.001$,**$p < 0.01$, *$p < 0.05$ versus the DMSO control.

FIG 11 Proposed mechanism through which EV71-induced cytosolic Ca^{2+} elevation affects the virus life cycle through SOCE activation and mitochondrial Ca^{2+} influx. EV71 2B caused ER Ca^{2+} depletion, resulting in SOCE activation. At 6 h p.i, cytosolic Ca^{2+} levels increased, causing a moderate elevation in mitochondrial Ca^{2+} and subsequent increases in mitochondrial electron transport chain complex (I through IV) activity and ATP generation for viral replication. At 12 h p.i, overloading of mitochondrial Ca^{2+} promoted viral release through apoptotic cell death triggered by the intrinsic apoptosis pathway. AnCoA4 and RR reduced the levels of cytosolic Ca^{2+} and mitochondrial Ca^{2+}, reducing viral replication and virus release, respectively. Oligomycin targets the mitochondrial complex V (ATP synthase), leading to inhibition of viral

replication. RR = ruthenium red. MCU = mitochondrial Ca^{2+} uniporter

688 **Tables**

689

TABLE 1 Enrichment analysis of biological processes using the DAVID in EV71-infected cells treated with AnCOA4 or left-untreated

Biological process	Gene (Entrez gene ID)[a]	*p*-value[b]
Electron transport coupled proton transport	MT-ND4, MT-ND5, MT-ND6, MT-CYB, MT-COI	3.15×10^{-3}
Mitochondrial electron transport, NADH to ubiquinone	MT-ND4L, MT-ND4, MT-ND5, MT-ND6	6.68×10^{-3}
ATP synthesis coupled electron transport	MT-ND4L, MT-ND4, MT-ND5, MT-ND6, MT-CYB, MT-COI	6.68×10^{-3}
Response to hydrogen peroxide	MT-ND4, MT-ND5, TXNIP	1.48×10^{-1}
Mitochondrial ATP synthesis coupled proton transport	MT-ND4L, MT-ND4, MT-ND5, MT-ND6, MT-CYB, MT-COI	1.41×10^{-2}
Positive regulation of transcription from RNA polymerase II promoter	CEBPB, KLF15, HOXA, NHLH1, NOG, RGCC, ZC3H12A	6.69×10^{-1}

[a] Gene ID obtained from Entrez Gene resource (https://www.ncbi.nlm.nih.gov/gene/) of NCBI

[b] *p*-values are adjusted by Bonferroni correction method, which multiplies the raw *p*-values.

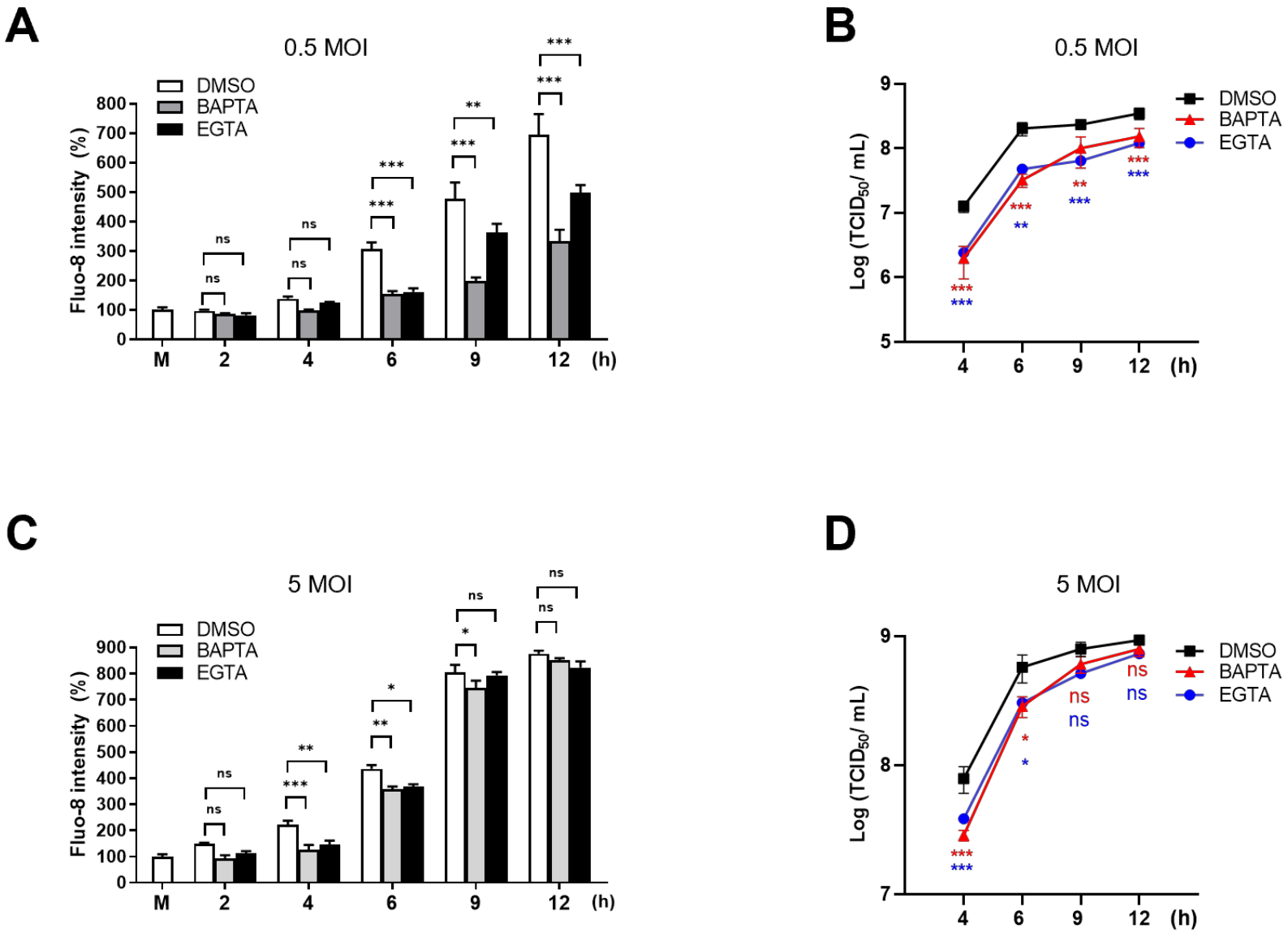
A
0.5 MOI
DMSO
BAPTA
EGTA
Fluo-8 intensity (%)
800
700
600
500
400
300
200
100
0
M
2
4
6
9
12
(h)
ns
***
**
B
0.5 MOI
Log (TCID50/ mL)
9
8
7
6
5
4
6
9
12
(h)
C
5 MOI
900
D
5 MOI

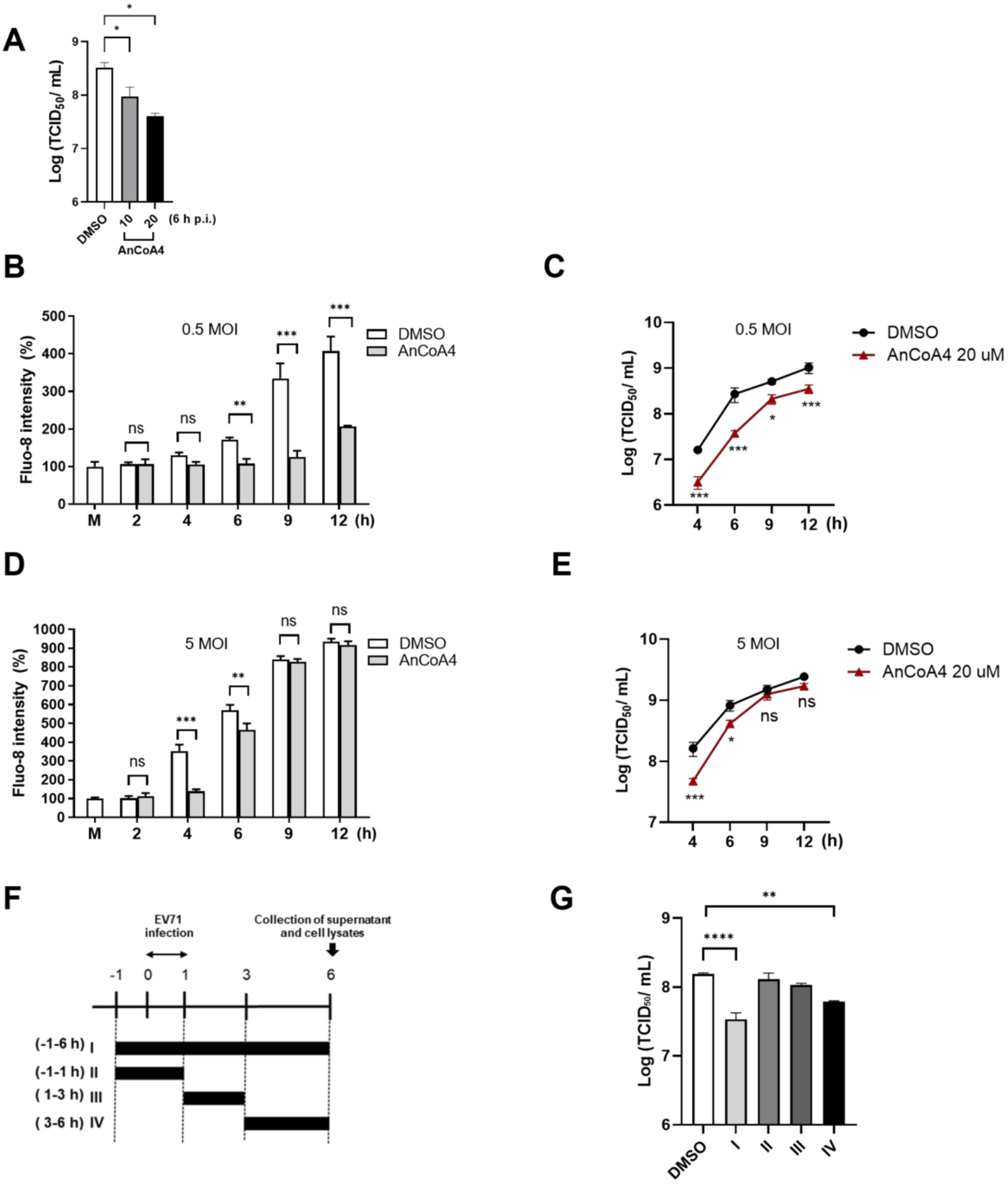
A
Log (TCID50/ mL)
DMSO
10
20
(6 h p.i.)
AnCoA4
B
0.5 MOI
Fluo-8 intensity (%)
DMSO
AnCoA4
ns
M
2
4
6
9
12 (h)
C
0.5 MOI
Log (TCID50/ mL)
DMSO
AnCoA4 20 uM
D
5 MOI
Fluo-8 intensity (%)
E
5 MOI
F
EV71 infection
Collection of supernatant and cell lysates
(-1-6 h) I
(-1-1 h) II
(1-3 h) III
(3-6 h) IV
G
Log (TCID50/ mL)
DMSO
I
II
III
IV

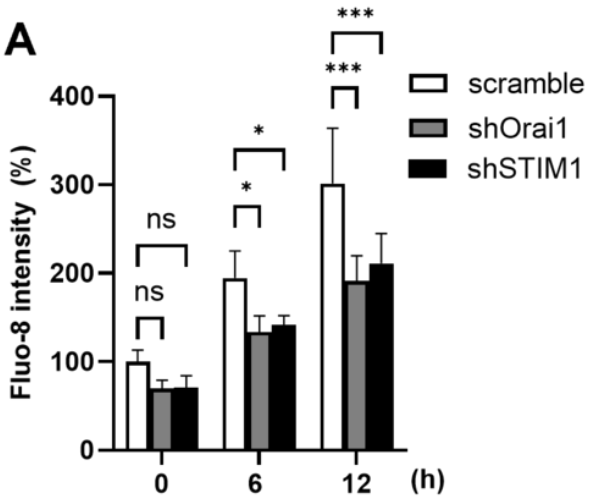
A
Fluo-8 intensity (%)
400
300
200
100
0
ns
ns
*
*
***
***
0
6
12
(h)
scramble
shOrai1
shSTIM1

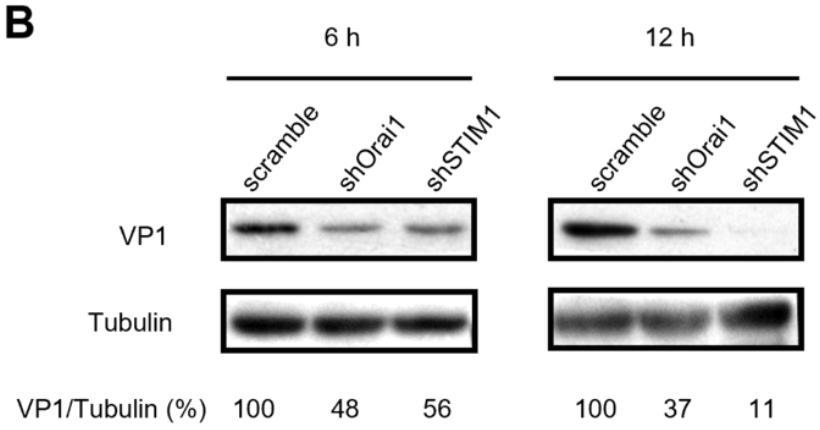
B
6 h
12 h
scramble
shOrai1
shSTIM1
scramble
shOrai1
shSTIM1
VP1
Tubulin
VP1/Tubulin (%)
100
48
56
100
37
11

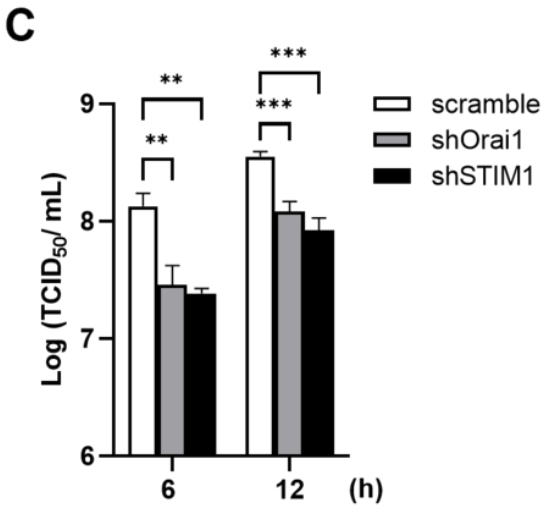
C
Log (TCID50/ mL)
9
8
7
6
**
**
***
***
6
12
(h)
scramble
shOrai1
shSTIM1

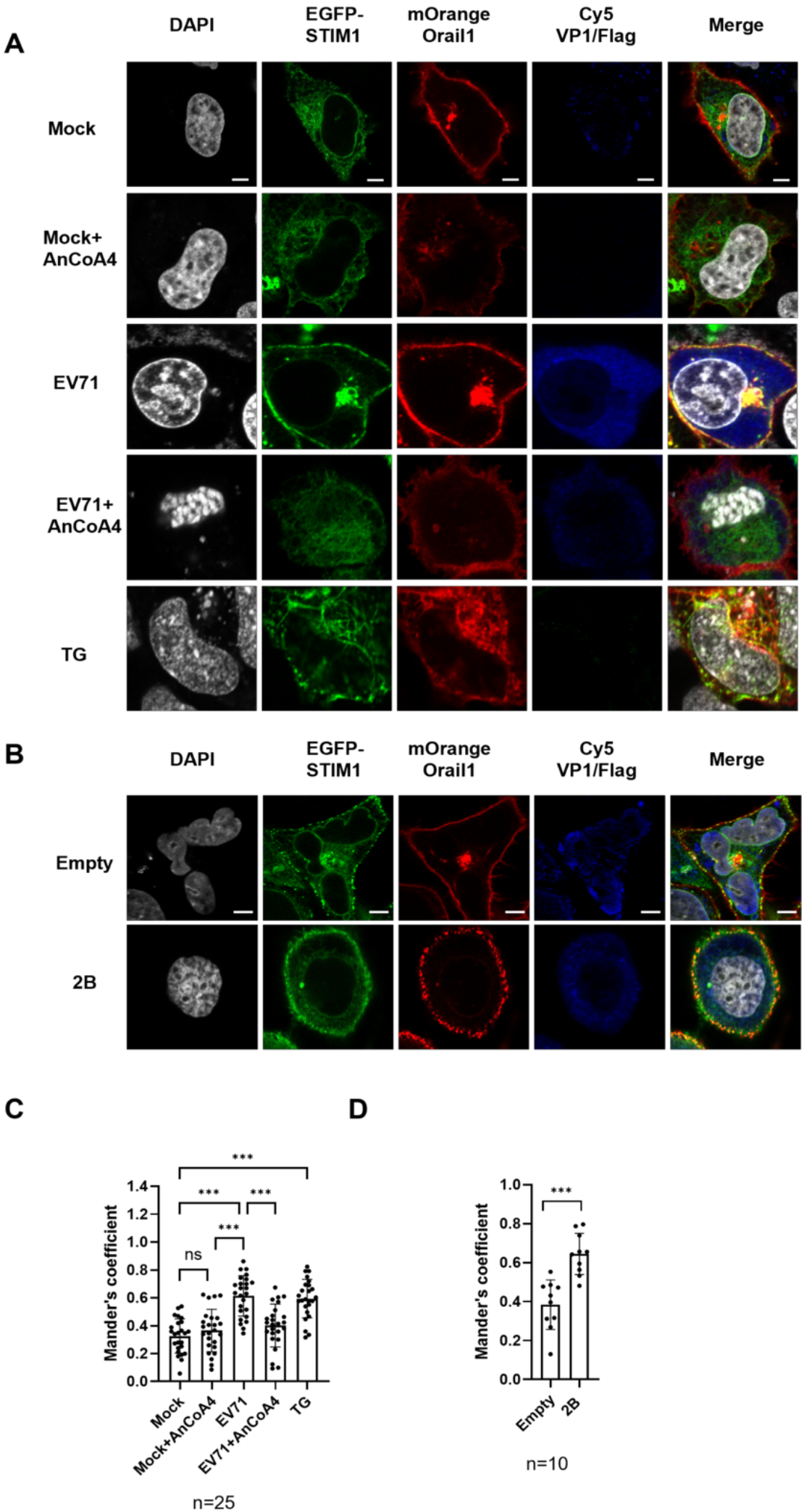
A
DAPI
EGFP-STIM1
mOrange Orail1
Cy5 VP1/Flag
Merge
Mock
Mock+ AnCoA4
EV71
EV71+ AnCoA4
TG
B
DAPI
EGFP-STIM1
mOrange Orail1
Cy5 VP1/Flag
Merge
Empty
2B
C
Mander's coefficient
1.4
1.2
1.0
0.8
0.6
0.4
0.2
0.0
***
***
***
***
ns
Mock
Mock+AnCoA4
EV71
EV71+AnCoA4
TG
n=25
D
Mander's coefficient
1.0
0.8
0.6
0.4
0.2
0.0
***
Empty
2B
n=10

A

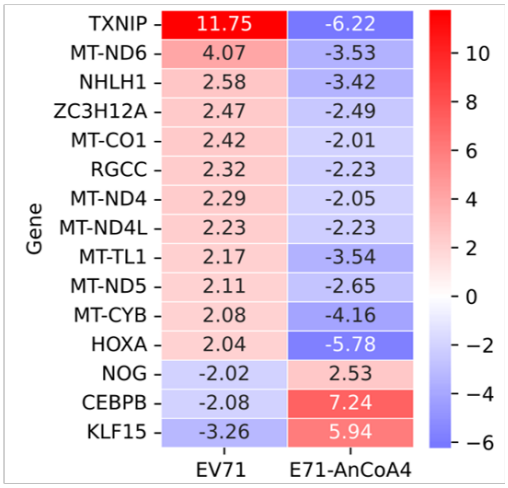
Gene
TXNIP 11.75 -6.22
MT-ND6 4.07 -3.53
NHLH1 2.58 -3.42
ZC3H12A 2.47 -2.49
MT-CO1 2.42 -2.01
RGCC 2.32 -2.23
MT-ND4 2.29 -2.05
MT-ND4L 2.23 -2.23
MT-TL1 2.17 -3.54
MT-ND5 2.11 -2.65
MT-CYB 2.08 -4.16
HOXA 2.04 -5.78
NOG -2.02 2.53
CEBPB -2.08 7.24
KLF15 -3.26 5.94
EV71
E71-AnCoA4
10
8
6
4
2
0
−2
−4
−6

B

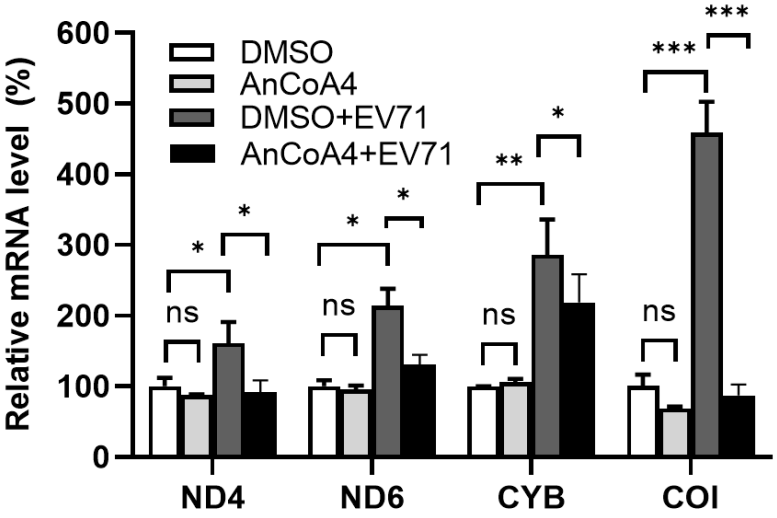
Relative mRNA level (%)
600
500
400
300
200
100
0
DMSO
AnCoA4
DMSO+EV71
AnCoA4+EV71
ns
*
**
***
ND4
ND6
CYB
COI

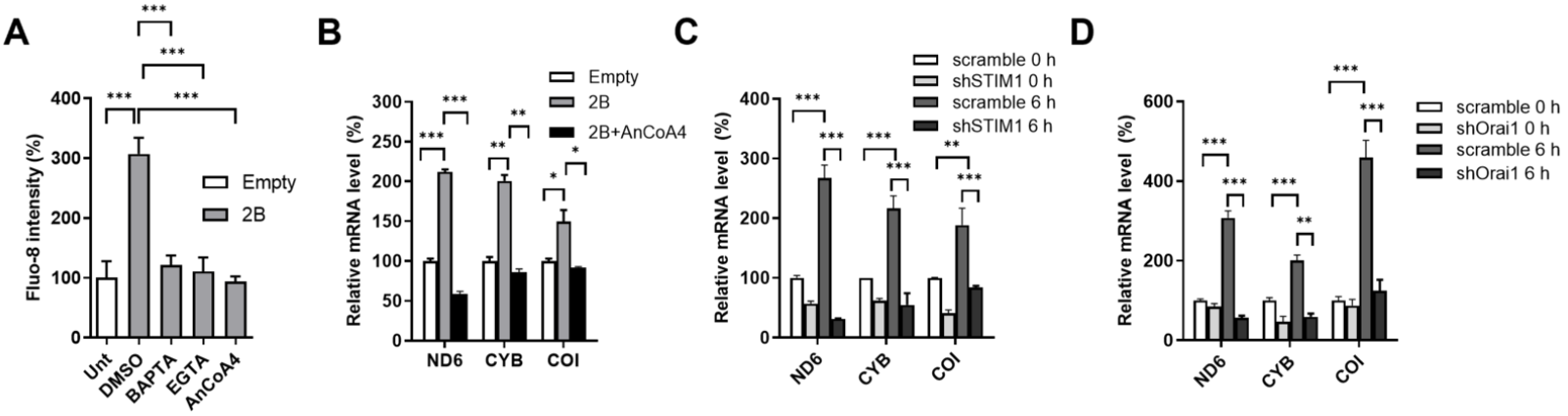
A
Fluo-8 intensity (%)
400
300
200
100
0
Empty
2B
Unt
DMSO
BAPTA
EGTA
AnCoA4
B
Relative mRNA level (%)
300
250
200
150
100
50
0
Empty
2B
2B+AnCoA4
ND6
CYB
COI
C
Relative mRNA level (%)
400
300
200
100
0
scramble 0 h
shSTIM1 0 h
scramble 6 h
shSTIM1 6 h
ND6
CYB
COI
D
Relative mRNA level (%)
600
400
200
0
scramble 0 h
shOrai1 0 h
scramble 6 h
shOrai1 6 h
ND6
CYB
COI

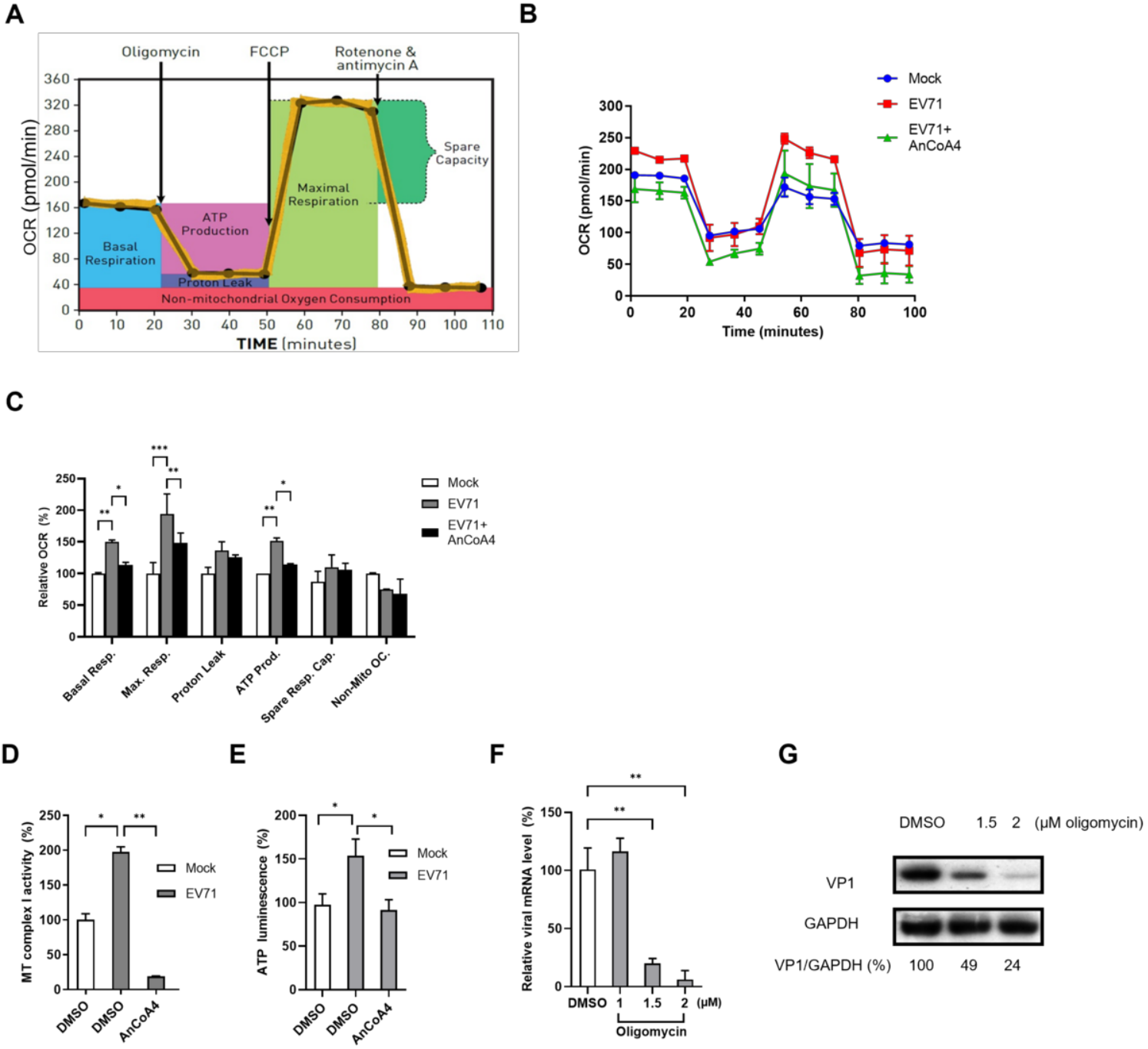
A
Oligomycin
FCCP
Rotenone & antimycin A
OCR (pmol/min)
Basal Respiration
ATP Production
Proton Leak
Maximal Respiration
Spare Capacity
Non-mitochondrial Oxygen Consumption
TIME (minutes)
B
Mock
EV71
EV71+ AnCoA4
OCR (pmol/min)
Time (minutes)
C
Relative OCR (%)
Mock
EV71
EV71+ AnCoA4
Basal Resp.
Max. Resp.
Proton Leak
ATP Prod.
Spare Resp. Cap.
Non-Mito OC.
D
MT complex I activity (%)
Mock
EV71
DMSO
DMSO
AnCoA4
E
ATP luminescence (%)
Mock
EV71
DMSO
DMSO
AnCoA4
F
Relative viral mRNA level (%)
DMSO
1
1.5
2 (μM)
Oligomycin
G
DMSO 1.5 2 (μM oligomycin)
VP1
GAPDH
VP1/GAPDH (%) 100 49 24

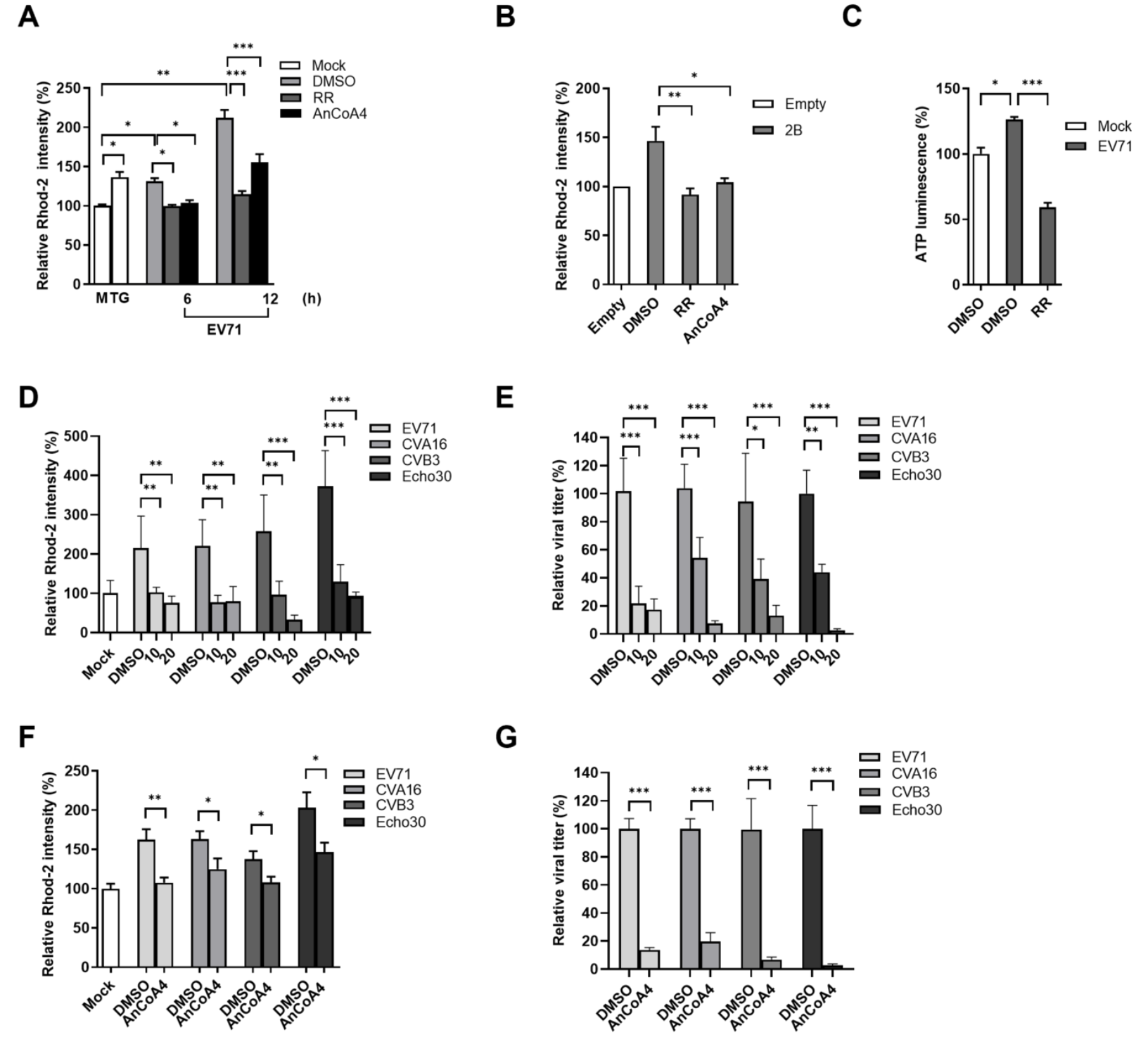
A
Relative Rhod-2 intensity (%)
Mock
DMSO
RR
AnCoA4
MTG
6
12
(h)
EV71
B
Relative Rhod-2 intensity (%)
Empty
2B
Empty
DMSO
RR
AnCoA4
C
ATP luminescence (%)
Mock
EV71
DMSO
DMSO
RR
D
Relative Rhod-2 intensity (%)
EV71
CVA16
CVB3
Echo30
Mock
DMSO
10
20
E
Relative viral titer (%)
EV71
CVA16
CVB3
Echo30
DMSO
10
20
F
Relative Rhod-2 intensity (%)
EV71
CVA16
CVB3
Echo30
Mock
DMSO
AnCoA4
G
Relative viral titer (%)
EV71
CVA16
CVB3
Echo30
DMSO
AnCoA4

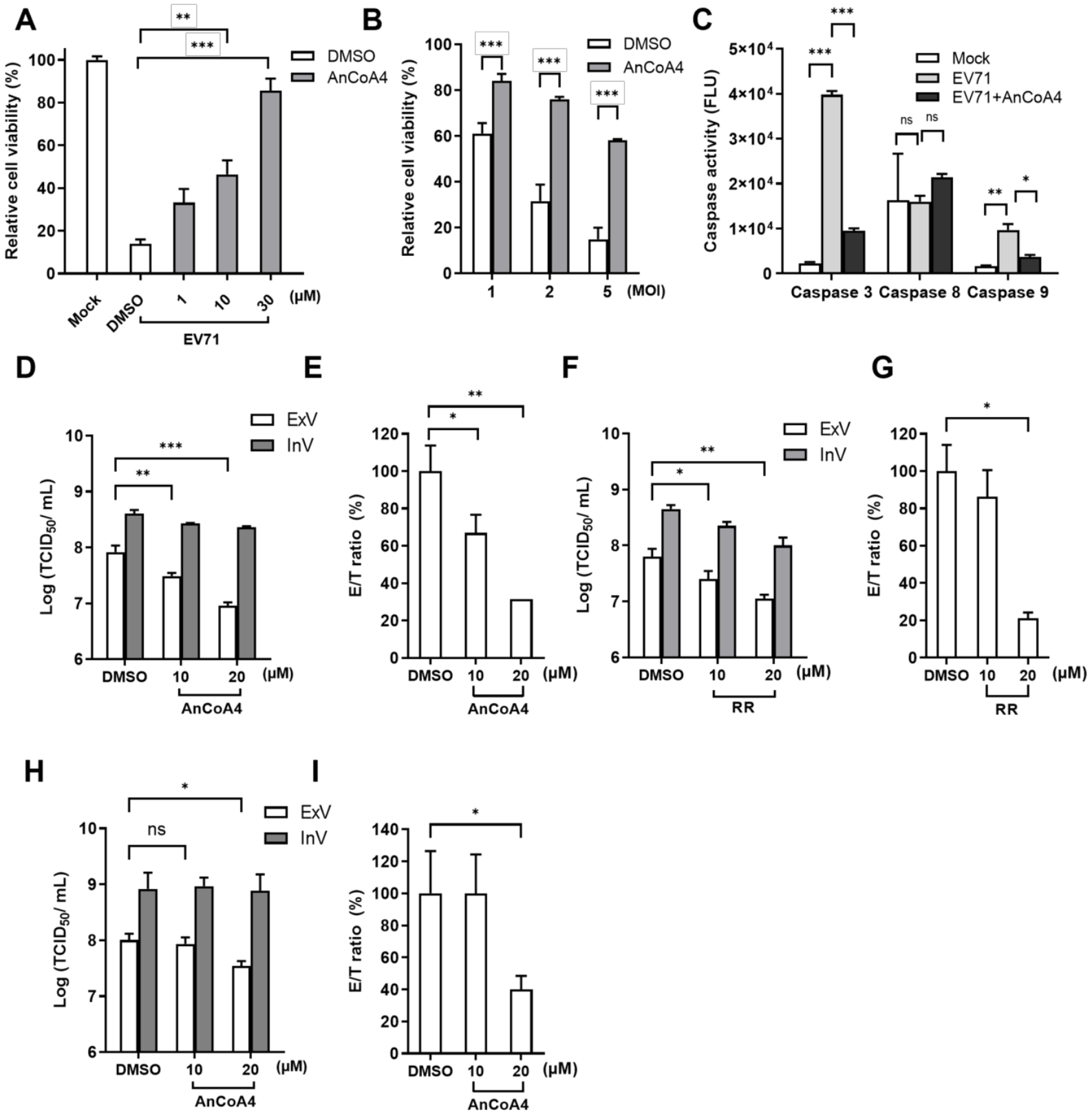
A
Relative cell viability (%)
DMSO
AnCoA4
Mock
DMSO
1
10
30
(μM)
EV71
B
Relative cell viability (%)
DMSO
AnCoA4
1
2
5
(MOI)
C
Caspase activity (FLU)
Mock
EV71
EV71+AnCoA4
Caspase 3
Caspase 8
Caspase 9
ns
D
Log (TCID50/ mL)
ExV
InV
DMSO
10
20
(μM)
AnCoA4
E
E/T ratio (%)
AnCoA4
F
Log (TCID50/ mL)
ExV
InV
RR
G
E/T ratio (%)
RR
H
Log (TCID50/ mL)
ExV
InV
ns
AnCoA4
I
E/T ratio (%)
AnCoA4

A

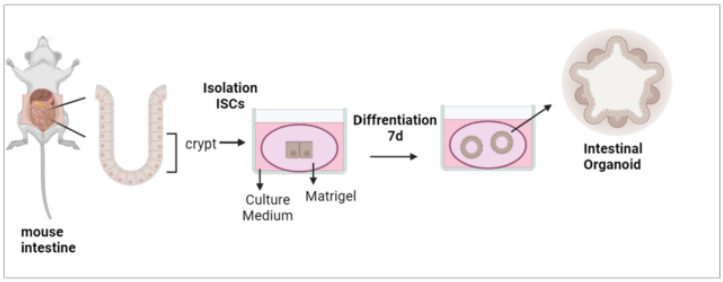
Isolation
ISCs
crypt
Culture
Medium
Matrigel
Diffrentiation
7d
Intestinal
Organoid
mouse
intestine

B

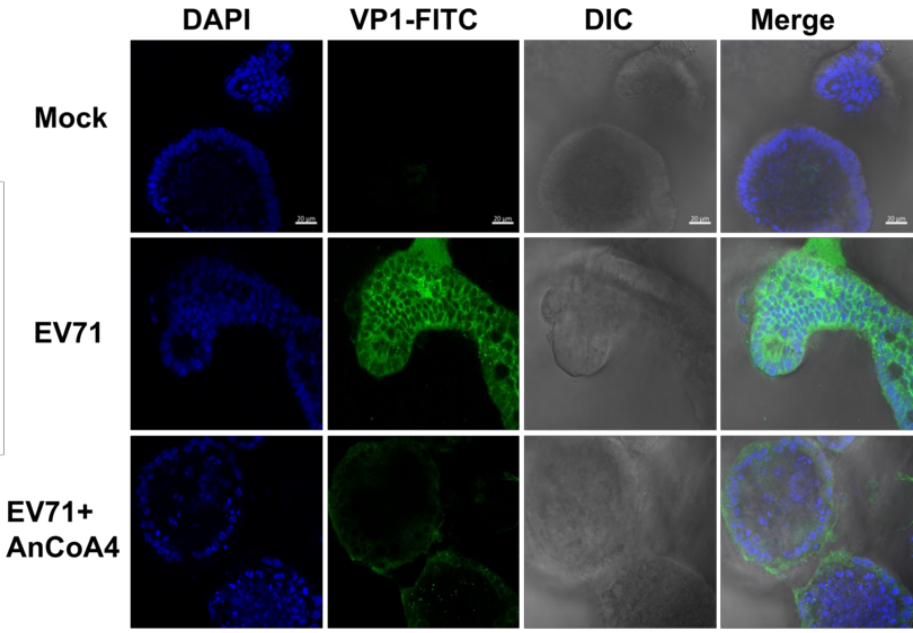
DAPI
VP1-FITC
DIC
Merge
Mock
EV71
EV71+
AnCoA4

C

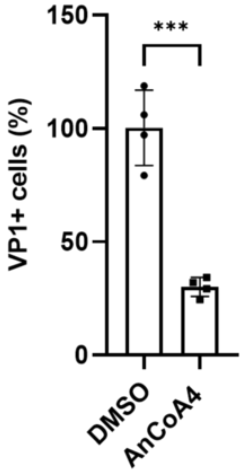
150
100
50
0
VP1+ cells (%)
***
DMSO
AnCoA4

D

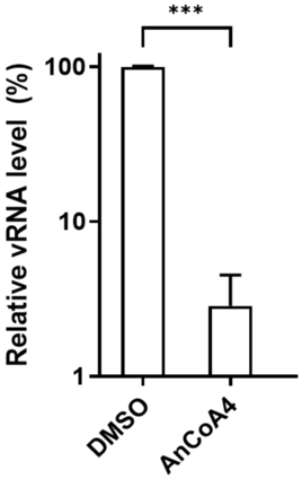
***
100
10
1
Relative vRNA level (%)
DMSO
AnCoA4

E

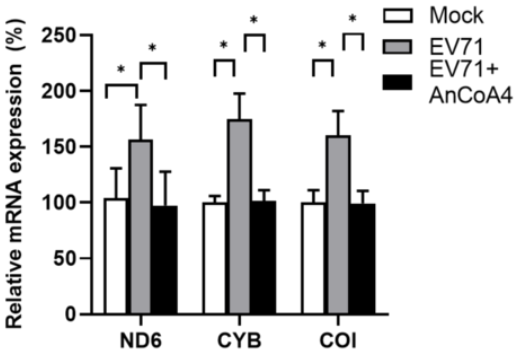
Mock
EV71
EV71+
AnCoA4
250
200
150
100
50
0
Relative mRNA expression (%)
*
ND6
CYB
COI

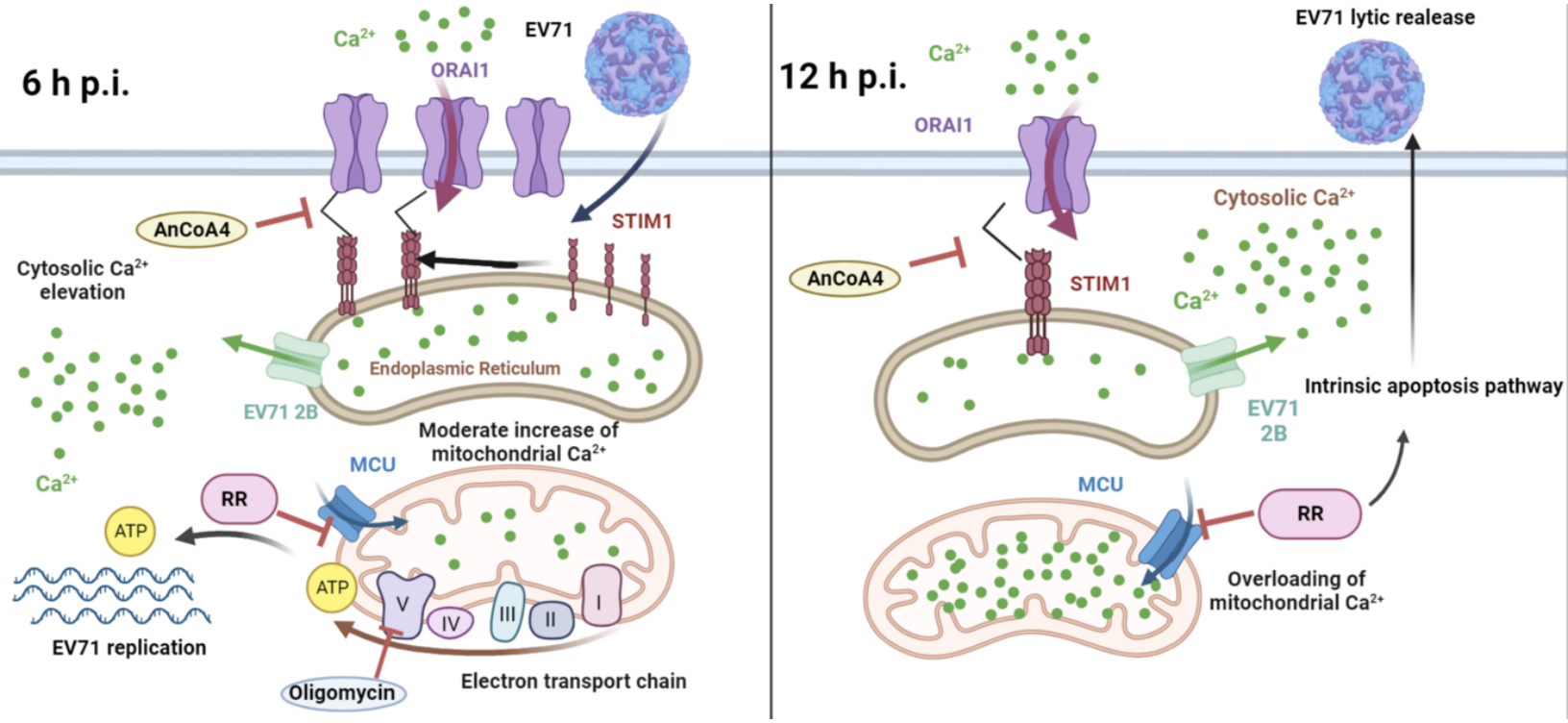
6 h p.i.
Ca2+
EV71
ORAI1
AnCoA4
STIM1
Cytosolic Ca2+ elevation
Endoplasmic Reticulum
EV71 2B
Moderate increase of mitochondrial Ca2+
MCU
Ca2+
RR
ATP
ATP
V
IV
III
II
I
EV71 replication
Oligomycin
Electron transport chain
12 h p.i.
Ca2+
EV71 lytic realease
ORAI1
Cytosolic Ca2+
AnCoA4
STIM1
Ca2+
Intrinsic apoptosis pathway
EV71 2B
MCU
RR
Overloading of mitochondrial Ca2+